

HistoAtlas: A Pan-Cancer Morphology Atlas Linking Histomics to Molecular Programs and Clinical Outcomes

Pierre-Antoine Bannier

We present HistoAtlas, a pan-cancer computational atlas that extracts 38 interpretable histomic features from 6,745 diagnostic H&E slides across 21 TCGA cancer types and systematically links every feature to survival, gene expression, somatic mutations, and immune subtypes. All associations are covariate-adjusted, multiple-testing corrected, and classified into evidence-strength tiers. The atlas recovers known biology, from immune infiltration and prognosis to proliferation and kinase signaling, while uncovering compartment-specific immune signals and morphological subtypes with divergent outcomes. Every result is spatially traceable to tissue compartments and individual cells, statistically calibrated, and openly queryable. HistoAtlas enables systematic, large-scale biomarker discovery from routine H&E without specialized staining or sequencing. Data and an interactive web atlas are freely available at <https://histoatlas.com>.

Keywords: digital pathology, computational pathology, cancer histomics, tumor morphology, pan-cancer atlas, whole slide image, tumor microenvironment

Correspondence: pierreantoine.bannier@gmail.com

1 Introduction

Histopathological examination of hematoxylin-and-eosin-stained (H&E) tissue sections remains the gold standard for cancer diagnosis (1, 2). Every diagnostic slide encodes quantitative information, from cell densities and nuclear morphology to spatial organization of immune infiltrates and stromal architecture (3). In existing pan-cancer resources, this information is collapsed into categorical grades or discarded entirely (4). Genomics (5), transcriptomics (6), proteomics (7), and epigenomics (8) each have mature pan-cancer resources that enable systematic cross-cancer comparison. Yet, histopathology, the most routinely generated cancer data modality, lacks an equivalent quantitative atlas.

The Cancer Genome Atlas (TCGA) established the paradigm for multi-omic integration across cancer types, cataloging somatic mutations, copy-number alterations, gene expression programs, and epigenetic landscapes (9). Thorsson et al. extended this framework to immune biology, defining six immune subtypes that stratify prognosis across 33 cancer types using transcriptomic and genomic features (10). Nonetheless, neither resource incorporates quantitative morphological data. This is a notable omission because the spatial context of immune infiltration carries prognostic information independent of molecular subtyping, as formalized in the Immunoscore (11–13). Saltz et al. mapped bulk tumor

infiltrating lymphocyte (TIL) density across 13 TCGA cancer types from deep-learning spatial maps (14), demonstrating the feasibility of pan-cancer morphological analysis from H&E. However, their approach reports a single bulk density score without compartment-specific resolution or linkage to gene expression programs.

Computational pathology has made rapid progress in extracting quantitative features from digitized slides (1). Early morphometric studies demonstrated that automated image features carry prognostic value in individual cancer types (15–17). Deep-learning classifiers now predict molecular alterations (18–20), microsatellite instability (21, 22), gene expression (23), and survival (24) directly from H&E with high accuracy. More recently, foundation models such as UNI (25), Virchow (26), or H0 (27), trained on large datasets of pan-tumor tissue via self-supervised learning, produce information-rich slide embeddings. Yet, these embeddings do not readily decompose into interpretable biological features such as cell densities, spatial distances, or tissue compartment fractions (4). In response to this interpretability gap, several groups have proposed explicit feature-based representations: Diao et al. (28) combined cell- and tissue-level predictions into hundreds of human-interpretable descriptors, and Abel et al. (29) derived large collections of nuclear morphometric features linked to genomic instability and prognosis. These studies show that interpretable H&E features carry rich biological signal, but their emphasis on large feature spaces does not naturally organize into a concise morphology atlas grounded in a small set of reproducible, compartment-resolved features.

Public resources mirror this gap: cBioPortal provides molecular data without morphology (30), TCIA hosts raw slides without precomputed features (31), and the Human Protein Atlas maps protein expression without quantitative morphometrics (32). These gaps leave cancer researchers without a resource that bridges morphology and molecular biology at pan-cancer scale. Such a resource would need to combine interpretable histomic features with systematic molecular linkage across cancer types, explicit multiple-testing control, and traceability from statistical associations back to tissue compartments and individual cells.

Here we present HistoAtlas, a pan-cancer morphology atlas built from 38 quantitative histomic features extracted from 6,745 TCGA diagnostic slides across 21 cancer types (plus a pooled pan-cancer analysis). We systematically test every feature for association with survival, gene expression, mutations, copy-number variation, and immune subtypes with explicit correction families and evidence-strength badges (strong, mod-

erate, suggestive, or insufficient). All results are released as a web atlas in which every association is spatially traceable to specific tissue compartments and individual cells (Fig. 6). We demonstrate that resolving immune cells by tissue compartment uncovers a stronger protective observational association between intratumoral lymphocyte density and survival than its stromal counterpart, a distinction diluted in bulk H&E-derived TIL scoring approaches. Among morphologically distinct clusters, morphology separates quiescent from hormone-driven subgroups with divergent outcomes.

2 Results

2.1 A quantitative atlas of cancer morphology

We constructed HistoAtlas from 6,745 H&E-stained diagnostic slides spanning 21 TCGA solid-tumor cancer types (Supplementary Table 3). Twelve additional cancer types were excluded because their dominant cell morphologies (lymphoid, glial, melanocytic, mesenchymal, neuroendocrine, renal tubular, or germ cell) fall outside the training domain of the segmentation models (Supplementary Table 3).

Two automated segmentation stages converted whole-slide images into quantitative measurements (§4.2). First, a UNet-based tissue segmentation model classified approximately 1.4 m² of tissue into five compartments (tumor [mean 44.9% of tissue area], stroma [45.4%], necrosis, blood, and normal epithelium; Fig. 1a), with tumor and stroma together accounting for over 90% of the analyzed area. Second, the HistoPLUS cell detection and classification model (33) identified more than 4.4 billion individual cells belonging to nine types: tumor cells, lymphocytes, fibroblasts, neutrophils, eosinophils, plasmocytes, apoptotic bodies, mitotic figures, and red blood cells.

From these segmentations we derived 38 histomic features organized into five categories: tissue composition, cell densities, nuclear morphology and kinetics, spatial organization, and spatial heterogeneity (definitions in Supplementary Table 1; descriptive statistics in Supplementary Table 10; preprocessing in §4.3).

We then tested each feature for associations with survival and molecular programs across all 22 cohorts. For survival, we fitted Cox proportional-hazards models for each combination of 38 features, 22 cohorts (21 cancer types plus a pan-cancer cohort), and four endpoints (overall, disease-specific, disease-free, and progression-free survival), yielding 5,623 evaluable associations (of a theoretical maximum of 6,688; the remainder were excluded for insufficient sample size or events) under two adjustment tiers, unadjusted and adjusted for age, sex, stage, and tissue source site (§4.4). After Benjamini–Hochberg correction within predefined correction families (§4.9; Supplementary Table 6), 260 associations were significant at a false discovery rate of 0.05. All 260 passed the proportional-hazards assumption (Schoenfeld $P \geq 0.05$; Supplementary Table 7), because associations with PH violations

have their Cox P -values invalidated before BH correction (§4.4); restricted mean survival time (RMST) summaries are provided as complementary measures for all associations.

For molecular associations, we computed 487,638 Spearman rank correlations between 38 histomic features and 293 molecular targets, comprising 133 curated cancer genes assessed for both mRNA expression and copy-number variation (Supplementary Table 4), 21 Hallmark pathway activity scores (of the 50 Hallmark gene sets, 21 had sufficient matched data), and 6 immune cell-fraction scores, across 22 cohorts under two adjustment tiers (§4.5). After family-wise Benjamini–Hochberg correction (Supplementary Table 6), 88,920 correlations (18.2%) were significant at a false discovery rate of 0.05, with the highest yield among immune cell fractions (39.2%), pathway scores (30.4%), and gene expression (24.9%), and the lowest among copy-number variation (6.3%) (Supplementary Table 11). Sample sizes vary across analyses because not all slides have matched molecular or clinical annotation; exact counts are reported per analysis throughout. The following subsections present what these associations show, beginning with a pan-cancer morphological landscape and progressing to compartment-resolved survival signals.

2.2 The pan-cancer morphological landscape recovers canonical biology

Our pipeline extracts 38 quantitative histomic features from each diagnostic H&E slide through automated tissue segmentation, cell detection, and spatial analysis (Fig. 1a). Pairwise Spearman correlation across all 6,745 slides revealed structured feature modules – density features form a tight positive-correlation block, morphology features cluster together, and cross-module anti-correlations delineate distinct biological axes (Fig. 1b) – confirming that the 38 features capture complementary aspects of tissue biology. To visualize the morphological landscape, we projected all 6,745 slides into a two-dimensional UMAP embedding computed from these features (§4.7; Fig. 1c). Cancer types occupied distinct regions of the embedding, with morphologically related types positioned adjacently: squamous carcinomas (HNSC, LUSC, CESC) clustered in a region of elevated nuclear pleomorphism, while hormone-driven adenocarcinomas (BRCA, PRAD) occupied a low-proliferation region. Unsupervised K-means clustering of the z-scored feature vector, without any molecular input, yielded 10 pan-cancer (L1) clusters (K selected by inspection of silhouette, Calinski–Harabasz, Davies–Bouldin, and gap statistic metrics; §4.7; Fig. 1d,e) and 69 cancer-specific (L2) subclusters. Bootstrap stability analysis (50 iterations, 80% subsamples) confirmed robust cluster assignments (mean adjusted Rand index = 0.72, Jaccard = 0.81). The adjusted Rand index between L1 clusters and cancer-type labels was 0.15, confirming that the clusters capture morphological variation that is not reducible to cancer-type identity.

Pathway and immune subtype enrichment analysis re-

vealed that these purely morphological clusters align with canonical molecular programs (§2.5). All pathway enrichments below are Cliff’s δ computed on Hallmark gene set scores (34) (Supplementary Table 5). Cluster 4 (76% THYM) exhibited strong immune rejection pathway enrichment ($\delta = 0.67$, 95% CI [0.60, 0.73], $P_{\text{adj}} = 3.3 \times 10^{-40}$), consistent with the active T-cell maturation environment that defines thymic biology (35, 36). Cluster 6 (61% COAD and READ) showed dominant Wnt/ β -catenin signaling ($\delta = 0.46$, 95% CI [0.42, 0.50], $P_{\text{adj}} = 1.3 \times 10^{-82}$) and C1 wound-healing immune subtype enrichment (OR = 5.59, 95% CI [4.69, 6.67], $P_{\text{adj}} = 1.1 \times 10^{-88}$), recapitulating the constitutive WNT activation that characterizes colorectal tumorigenesis (37). Cluster 8 (44% BRCA, 24% PRAD) displayed estrogen response upregulation ($\delta = 0.52$, 95% CI [0.49, 0.56], $P_{\text{adj}} = 2.2 \times 10^{-160}$) and proliferation suppression ($\delta = -0.51$, 95% CI [-0.54, -0.48], $P_{\text{adj}} = 3.8 \times 10^{-154}$), consistent with the hormone-driven, genomically quiet phenotype of luminal breast and prostate cancers (9, 38). The algorithm received no molecular input, yet grouped thymomas by immune rejection pathways, colorectal cancers by WNT activation, and hormone-driven tumors by estrogen response.

Because L1 clusters dominated by a single cancer type could trivially inherit that type’s molecular profile, we examined two additional lines of evidence. First, Cluster 3 ($n = 1,012$) spans five cancer types with no dominant contributor (HNSC 17.7%, STAD 17.2%, BLCA 14.3%, LUSC 14.3%, LUAD 11.8%) yet showed coherent enrichment for hypoxia ($\delta = 0.34$, 95% CI [0.30, 0.38], $P_{\text{adj}} = 1.7 \times 10^{-57}$), interferon- γ response ($\delta = 0.46$, 95% CI [0.43, 0.49], $P_{\text{adj}} = 1.3 \times 10^{-105}$), and C2 (IFN- γ dominant) immune subtype (OR = 2.74, 95% CI [2.37, 3.17], $P_{\text{adj}} = 2.1 \times 10^{-40}$). Second, within-cancer (L2) subclusters showed biology beyond cancer-type identity: within BRCA alone, subcluster 2 ($n = 280$) was enriched for C2 immune subtype (OR = 4.86, 95% CI [3.58, 6.59], $P_{\text{adj}} = 8.1 \times 10^{-25}$) and interferon- γ response ($\delta = 0.47$, 95% CI [0.39, 0.54], $P_{\text{adj}} = 3.8 \times 10^{-28}$), while subcluster 3 ($n = 325$) showed estrogen response enrichment ($\delta = 0.26$, 95% CI [0.19, 0.34], $P_{\text{adj}} = 1.2 \times 10^{-9}$) and depletion across all six immune pathways. These within-cancer results confirm that the histomic features capture biological heterogeneity not reducible to cancer-type identity. The remaining clusters and their survival associations are detailed in §2.5.

2.3 Spatial immune topology is associated with survival in a compartment-specific manner

Unlike bulk TIL scoring approaches (14, 39), HistoAtlas quantifies immune cell density, spatial proximity, and infiltration patterns separately in the intratumoral, stromal, and invasive front compartments. All survival associations in this subsection use Cox regression adjusted for age, sex, stage, and stratified by tissue source site for overall survival (§4.4; pan-cancer models additionally stratified by cancer type).

Pan-cancer analysis revealed compartment-specific differences in prognostic strength (Fig. 2a). Intratumoral lymphocyte density was associated with favorable outcomes (pan-cancer hazard ratio [HR] = 0.87, 95% CI [0.81, 0.93], $P_{\text{adj}} = 9.8 \times 10^{-4}$, $n = 4,560$), whereas stromal lymphocyte density showed a weaker, attenuated protective effect (HR = 0.89, 95% CI [0.83, 0.97], $P_{\text{adj}} = 0.031$, $n = 4,561$). Intratumoral lymphocyte density showed a protective direction (HR < 1) in 11 of 17 evaluable cancer types, with BRCA exhibiting the strongest effect (HR = 0.72, 95% CI [0.60, 0.88], $P_{\text{adj}} = 0.018$, $n = 960$; Fig. 2b) followed by HNSC (HR = 0.74, 95% CI [0.63, 0.87], $P_{\text{adj}} = 3.9 \times 10^{-3}$, $n = 444$). In BRCA, stromal lymphocyte density showed a weaker, non-significant association (HR = 0.93, 95% CI [0.77, 1.12], $P_{\text{adj}} = 0.67$), indicating that the intratumoral compartment carries the dominant prognostic signal (Fig. 6b). Aggregate TIL scores that combine both compartments dilute this compartment-specific effect.

Spatial proximity features provided an additional prognostic axis. Tumor-lymphocyte nearest-neighbor distance at the invasive front, a spatial measure of immune exclusion (40, 41), inversely correlated with CD8A expression in BRCA ($\rho = -0.53$, $P_{\text{adj}} = 1.8 \times 10^{-68}$, $n = 958$; Fig. 2c).

Gene-level correlations validated the biological identity of these features. In BRCA, intratumoral lymphocyte density correlated with cytotoxic T-cell markers and immune checkpoint genes (CD8A: $\rho = 0.59$, 95% CI [0.54, 0.63]; TIGIT: $\rho = 0.63$, 95% CI [0.59, 0.67]; both $P_{\text{adj}} < 10^{-85}$, $n = 958$; Fig. 2d). These features also discriminated Thorsson immune subtypes (10): peritumoral immune richness (the number of distinct immune cell types detected within 50 μm of the tumor boundary; Supplementary Table 1) explained 13% of immune subtype variance (Kruskal–Wallis $\eta^2 = 0.13$, 95% CI [0.12, 0.15], $P_{\text{adj}} = 3.0 \times 10^{-159}$, $n = 5,590$; pan-cancer), consistent with concordance between histomic and transcriptomic immune classifications. A composite feature, interface-normalized immune pressure (lymphocyte count within 50 μm of the tumor–stroma boundary divided by interface length, cells mm^{-1} ; Supplementary Table 1), was protective in HNSC (HR = 0.74, 95% CI [0.63, 0.86], $P_{\text{adj}} = 3.9 \times 10^{-3}$, $n = 444$; a value similar to intratumoral lymphocyte density, reflecting the high correlation between these features).

Additional features showed consistent protective trends across cancer types. Lymphocyte density spatial heterogeneity was protective in 14 of 17 evaluable cancer types (unadjusted model). The unadjusted associations for interface-normalized immune pressure in BRCA (HR = 0.72, $P_{\text{adj}} = 7.6 \times 10^{-3}$) and LIHC (HR = 0.79, $P_{\text{adj}} = 0.038$) did not survive covariate adjustment.

2.4 Morphometric features encode molecular programs

We next tested whether purely morphometric features serve as proxies for molecular programs. Of the 487,638 histomic–molecular correlations (§2.1), 88,920 (18.2%) were significant

at $FDR < 0.05$. Under a permutation null model (100 shuffles of molecular labels within each cancer type, with per-cancer-type BH correction matching the production pipeline), 0% of pairs were significant at the same threshold, confirming that the observed 18.2% discovery rate reflects genuine biological signal rather than statistical artifact (Supplementary Methods). The correlation structure was biologically coherent: immune density features correlated with immune pathway signatures, proliferation features with cell cycle pathways, and invasion features with epithelial-mesenchymal transition (EMT) scores (Fig. 3a). Among significant pairs, the median absolute ρ was 0.18 (IQR 0.13–0.27). Fig. 3b shows the distribution of effect sizes for pan-cancer adjusted-model associations, stratified by molecular data type: gene expression (4,371/5,453 significant, 80%), Hallmark pathways (1,692/2,050, 83%), and copy-number variation (2,845/5,453, 52%).

Three examples from breast cancer (BRCA, $n = 958$; unadjusted model) illustrate the strength of this morphology-to-molecular correspondence. First, mitotic index correlated with canonical proliferation markers (PLK1: $\rho = 0.56$, 95% CI [0.51, 0.61], $P_{adj} = 5.2 \times 10^{-77}$; additional markers including AURKA, MKI67, CCNB1, and TOP2A). Second, invasion depth showed modest correlations ($|\rho| = 0.25$ –0.32) consistent with the classical EMT axis (42), with ZEB1 as the strongest correlate ($\rho = 0.32$, 95% CI [0.26, 0.37], $P_{adj} = 8.4 \times 10^{-23}$) and an inverse correlation with the epithelial marker CDH1 ($\rho = -0.25$, 95% CI [-0.32, -0.19], $P_{adj} = 1.0 \times 10^{-14}$). Third, nuclear pleomorphism anti-correlated with luminal differentiation markers (BCL2: $\rho = -0.37$, 95% CI [-0.43, -0.32], $P_{adj} = 8.1 \times 10^{-32}$; ESR1: $\rho = -0.36$, 95% CI [-0.41, -0.30], $P_{adj} = 4.4 \times 10^{-29}$), consistent with the histological grading criteria of Elston and Ellis (43). The mitotic index–PLK1 correspondence generalized across cancer types (LUAD: $\rho = 0.65$, $n = 437$; LIHC: $\rho = 0.60$, $n = 348$; pan-cancer: $\rho = 0.68$, $n = 5,875$; all $P_{adj} < 10^{-27}$).

Invasion depth also inversely correlated with cell cycle pathway scores in BRCA ($\rho = -0.30$, 95% CI [-0.36, -0.25], $P_{adj} = 4.6 \times 10^{-21}$, $n = 957$). This slide-level inverse association between invasion and proliferation is consistent with the “go-or-grow” hypothesis (44, 45), although it cannot establish single-cell-level mutual exclusivity. Together, these correspondences confirm that histomic features capture interpretable aspects of known biological programs, providing a morphology-to-molecular bridge that operates without specialized staining or sequencing.

2.5 Morphological clusters define molecular archetypes

Beyond the pathway enrichments that independently recovered canonical biology (§2.2), the 10 L1 clusters also carried distinct mutational and immune subtype profiles (Fig. 4a,b). Mutation enrichment analysis (Fisher’s exact test, $FDR < 0.05$) showed Cluster 6 (61% CRC) enriched for TTN (odds ratio [OR] = 1.91, 95% CI [1.58, 2.31],

$P_{adj} = 1.4 \times 10^{-9}$), FAT4 (OR = 1.91, 95% CI [1.46, 2.49], $P_{adj} = 4.9 \times 10^{-5}$), and SYNE1 (OR = 1.86, 95% CI [1.47, 2.35], $P_{adj} = 1.1 \times 10^{-5}$), mutations frequently observed in colorectal genomes. Cluster 8 (44% BRCA, 24% PRAD) was depleted for chromatin modifier mutations (KMT2D OR = 0.42, 95% CI [0.31, 0.55], $P_{adj} = 5.8 \times 10^{-11}$; ZFX4 OR = 0.44, 95% CI [0.33, 0.58], $P_{adj} = 4.8 \times 10^{-10}$), consistent with a genomically quiet, hormone-driven phenotype. Because cluster molecular enrichments partly reflect cancer-type composition (e.g., Cluster 4 is 76% THYM), within-cancer-type (L2) enrichments that control for this confound are available in the web atlas.

Cluster-level survival analysis used Cox regression stratified by cancer type (Fig. 1d). This analysis revealed a prognostically important distinction among morphologically distinct clusters. Cluster 2 ($n = 607$; 44% LIHC, 28% THCA) displayed profoundly quiescent morphology: proliferation pathway scores were suppressed relative to all other slides (Cliff’s $\delta = -0.58$, $P_{adj} = 4.2 \times 10^{-102}$; E2F targets), and it showed favorable survival (HR = 0.54, 95% CI [0.40, 0.73], $P_{adj} = 6.3 \times 10^{-4}$; $n = 516$ with events). Cluster 5 ($n = 488$; 25% ACC, 20% BRCA) showed immune spatial exclusion (depleted cytotoxic immune activity; Cliff’s $\delta = -0.54$, $P_{adj} = 2.3 \times 10^{-62}$; allograft rejection) with near-average proliferative activity, and a non-significant adverse trend (HR = 1.17, 95% CI [0.96, 1.42], $P_{adj} = 0.28$).

Thorsson immune subtype (10) composition further distinguished the two clusters. Cluster 5 was enriched for C4 (lymphocyte depleted; OR = 5.49, 95% CI [4.23, 7.11], $P_{adj} = 2.8 \times 10^{-30}$; 28% of slides) and depleted for C2 (IFN- γ dominant; OR = 0.48, $P_{adj} = 3.9 \times 10^{-8}$). Cluster 2 showed combined C4 (OR = 7.14, 95% CI [5.72, 8.93], $P_{adj} = 1.3 \times 10^{-56}$) and C3 (inflammatory; OR = 4.99, 95% CI [4.13, 6.02], $P_{adj} = 1.6 \times 10^{-60}$) enrichment (85% combined; Fig. 4a). Although C3 is labeled “inflammatory,” Cluster 2’s morphology was uniformly quiescent, with suppressed lymphocyte density and proliferative indices, suggesting that its C3-classified tumors represent a quiescent inflammatory state rather than active immune engagement. Immune subtype labels alone classified both clusters as immune-depleted variants but did not distinguish their divergent proliferative states; the morphological axis of quiescent-cold versus hormone-driven tumors added prognostic information that transcriptomic subtyping did not capture.

Cluster 8 (BRCA/PRAD, hormone-driven) showed adverse survival (HR = 1.37, 95% CI [1.15, 1.62], $P_{adj} = 1.8 \times 10^{-3}$, $n = 1,112$). The remaining clusters did not reach significance after BH correction. Hazard ratios and P -values for all 10 clusters are shown in Fig. 1d.

2.6 Reporting what the atlas detects and what it cannot

HistoAtlas accompanies every association with Benjamini–Hochberg-corrected (46) P -values, bootstrap confidence in-

tervals, effect sizes, and evidence-strength badges (Fig. 5; statistical details in §4.9–4.11).

We assessed batch effects from tissue source site (TSS) using principal variance component analysis (PVCA) (47) and silhouette scores. At the pan-cancer level, PVCA attributed 44.7% of feature variance to TSS, 32.7% to cancer-type identity, and 22.6% to residual (Fig. 5a). Because TSS is partially confounded with cancer type (most sites contribute primarily one cancer type), the 44.7% TSS component includes both genuine institutional variation and cancer-type-associated morphological differences. Within individual cancer types, where batch effects could confound feature–outcome associations, per-cancer-type batch variance ranged from 2.7% (ACC) to 29.1% (ESCA), and all 20 per-cancer silhouette scores by TSS were negative (range -0.18 to -0.0004 ; one cancer type [CHOL] was excluded from per-cancer batch QC due to insufficient TSS diversity), indicating that no cancer type exhibited TSS-driven sub-clustering.

Spearman correlation P -values use the analytical t -test approximation ($t = r\sqrt{df/(1-r^2)}$; §4.5), validated by near-perfect concordance with a permutation-based reference ($\rho > 0.999$, $n = 282,278$ pairs). As a calibration check, we verified that raw P -values for the weakest-signal features (those with median effect size in the bottom quartile) followed an approximately uniform distribution, consistent with the null expectation.

To quantify what the atlas *cannot* detect, we computed the minimum detectable effect size (MDES) at 80% power for every analysis, using the Schoenfeld–Freedman approximation (48, 49) for survival associations and the Fisher z -transform for correlations. MDES varies across cancer types because sample sizes and event counts differ: well-powered cancer types such as BRCA ($n = 960$ for OS, 135 events) can detect hazard ratios as small as 1.62, whereas underpowered types such as cholangiocarcinoma (CHOL, $n = 36$) require hazard ratios exceeding 3.75 (Fig. 5b).

Each association receives an evidence-strength badge (strong, moderate, suggestive, or insufficient) computed from adjusted P -value, effect size magnitude, confidence interval width, and sample size (§4.11). Across 5,623 survival associations (38 features \times 22 cohorts \times 4 endpoints \times 2 adjustment tiers, excluding combinations with insufficient data), 33 (0.6%) achieved strong evidence, 167 (3.0%) moderate, 577 (10.3%) suggestive, and 4,846 (86.2%) insufficient. The predominance of insufficient evidence reflects the limited statistical power of smaller cohorts: most insufficient-evidence pairs involve cancer types with $n < 100$, where MDES exceeds clinically meaningful thresholds (Fig. 5b). The 33 strong and 167 moderate associations span multiple cancer types and all five feature categories, providing a curated set of high-confidence findings. Cross-endpoint replication rates for DSS, DFS, and PFS are discussed in Supplementary Note 2.

3 Discussion

HistoAtlas demonstrates that interpretable, spatially resolved histomic features extracted from routine H&E slides recapitulate canonical molecular programs, including proliferation kinase networks, EMT transcriptional axes, and immune cell gene signatures (Fig. 3), while stratifying clinical outcomes across cancer types. The central advance is not any single association but the comprehensive, statistically transparent linking of 38 quantitative features to survival, gene expression, mutations, and immune subtypes at pan-cancer scale. We deliver this linking as an openly queryable resource.

A systematic biological plausibility audit (Supplementary Table 2) decomposed atlas findings into 60 atomic claims and assessed each against the literature. Of these, 42 (70%) are well-established or supported by prior studies (11–13, 42, 44, 45, 50–54), 12 (20%) are novel but biologically plausible, 5 (8%) are novel with uncertain mechanisms, and 1 (2%) is an apparent contradiction that was resolved upon examination: spatial composition heterogeneity does not equate to genetic clonal diversity (55) (Supplementary Table 2). No claim contradicted established biology, a necessary consistency check for the feature extraction and statistical framework.

Several atlas-enabled findings warrant targeted follow-up. The compartment-specific difference in prognostic strength between intratumoral and stromal lymphocyte density (strong versus weak protection, respectively; Fig. 2a) is consistent with the importance of immune cell localization within the tumor microenvironment (13, 40, 41, 56). Saltz et al. scored bulk TIL density across 13 TCGA cancer types from deep-learning maps (14) but did not distinguish intratumoral from stromal compartments. To our knowledge, the differential prognostic contribution of these compartments had not been quantified across 21 cancer types from H&E morphometrics. We also identified morphologically distinct clusters with divergent survival outcomes: quiescent-cold (Cluster 2; hazard ratio = 0.54) versus hormone-driven (Cluster 8; hazard ratio = 1.37; Fig. 1d). This finding suggests that the binary immune-hot/immune-cold classification (56) may obscure biologically and potentially clinically relevant heterogeneity. Additional novel features showed consistent prognostic signals: lymphocyte density spatial heterogeneity (coefficient of variation across tiles) was protective in 14 of 17 evaluable cancer types (unadjusted model) and may proxy tertiary lymphoid structure formation (57); interface-normalized immune pressure, a composite measure of immune cell engagement at the tumor-stroma boundary, was protective in HNSC (hazard ratio = 0.74, $P_{\text{adj}} = 3.9 \times 10^{-3}$); the unadjusted associations previously observed in BRCA and LIHC did not survive covariate adjustment. TCGA lacks immunotherapy response data, so the clinical relevance of these immune distinctions for treatment selection remains speculative. All findings are hypothesis-generating; none should be interpreted as established biomarkers without independent confirmation.

Evaluating these findings in context requires comparing HistoAtlas to existing cancer data resources. cBioPortal (30)

provides comprehensive molecular and clinical data but lacks any morphological features. The Human Protein Atlas (32) provides semi-quantitative protein expression scores from immunohistochemistry with cancer-specific survival associations (58), but does not extract continuous morphometric features from H&E-stained sections or link them to molecular programs beyond single-protein correlations. The Cancer Imaging Archive (31) hosts raw imaging data without a statistical layer. Individual computational pathology studies have linked H&E features to outcomes in single cancer types (15, 16), and Diao et al. extracted 607 human-interpretable features across five cancer types (28), but most recent approaches rely on deep-learning embeddings that do not decompose into named histological features (25, 26). HistoAtlas addresses this interpretability gap: a tissue segmentation overlay with nine spatial zones derived from five tissue compartments, and cell-type annotations for nine morphological cell types enable users to trace any statistical finding to specific tissue regions and verify the underlying cell predictions visually (Fig. 6a–d).

Three categories of limitation constrain the current atlas. *Data scope*: all 6,745 slides derive from TCGA, a retrospective convenience cohort with institutional selection biases (59). We include 21 of 33 available cancer types; the 12 excluded types harbor dominant cell populations (lymphoid, glial, melanocytic, mesenchymal, neuroendocrine, renal tubular, or germ cell) outside the segmentation model’s training domain (Supplementary Table 3). TCGA participants are predominantly of European ancestry (9, 59); generalizability to diverse populations remains untested. Treatment standards have evolved since TCGA accrual (2000–2016), limiting applicability to contemporary regimens. *Feature quality*: because 13 of 21 cancer types are out-of-distribution for the cell segmentation model (trained on eight cancer types; §4.2), feature reliability varies across the atlas, and certain cancers (PRAD, LIHC, THCA) show elevated mitotic and apoptotic indices from reduced cell detection. Seven ratio features required winsorization to mitigate gate loophole artifacts, distance features are quantized at $8 \mu\text{m px}^{-1}$ resolution, and two tissue-model features carry zero signal. We use one slide per case, sacrificing assessment of intratumoral heterogeneity. *Analytical constraints*: all survival models test one histomic feature at a time alongside clinical covariates; a penalized multivariate model (e.g., LASSO Cox) would identify which features carry independent prognostic information and is a natural next step. Several features are correlated by construction (e.g., density features sharing the same denominator region), so the effective number of independent features is lower than 38. Morphology-to-molecular correlations are modest in magnitude (median significant $|\rho| = 0.18$, IQR 0.13–0.27); the features serve as noisy proxies for, not replacements of, molecular measurements. *Validation gap*: we have not performed external replication. All associations are internal to TCGA, and independent confirmation in CPTAC (7) or METABRIC (60) cohorts is required before any clinical interpretation. We have

not benchmarked interpretable features against whole-slide foundation model embeddings (25, 26); a direct comparison of predictive power versus interpretability would strengthen the case for handcrafted features but requires a dedicated study.

Three extensions would substantially strengthen the atlas. Overlaying spatial transcriptomics data (Visium, MERFISH) onto histomic features would provide gold-standard validation for spatial immune metrics and could calibrate morphometric proxies against measured transcript distributions. Integrating foundation model embeddings alongside interpretable histomic features would enable direct comparison of interpretability versus predictive power. Extending the framework to non-TCGA cohorts would test generalizability and enable community-contributed cancer types.

We designed HistoAtlas for transparency and reuse. Every association carries an evidence-strength badge (strong, moderate, suggestive, or insufficient) computed from adjusted P values, effect sizes, confidence interval widths, and sample sizes. The atlas reports the minimum detectable effect size at 80% power, conveying not only what it finds but also what it cannot detect. Bidirectional spatial traceability links every population-level statistic to tissue compartment maps and individual cell annotations on the original slide, and from any slide back to population-level associations (Fig. 6c,d). By making every morphological association traceable, statistically calibrated, and openly queryable by humans and machines alike, HistoAtlas provides infrastructure for systematic morphology-aware cancer analyses. All analysis code, feature metadata, and precomputed results are publicly released.

4 Methods

4.1 Data acquisition

We obtained formalin-fixed, paraffin-embedded (FFPE) hematoxylin and eosin (H&E)-stained diagnostic whole-slide images from The Cancer Genome Atlas (TCGA) via the Genomic Data Commons (GDC) portal for 21 solid-tumor cancer types (Supplementary Table 3). Slides were excluded if the viable tissue area fell below 1 mm^2 , if severe processing artifacts (pen marks covering $>20\%$ of tissue area, out-of-focus regions) were present, or if essential clinical metadata (vital status, follow-up time) was missing. To avoid pseudo-replication, we retained one slide per case: for each case with multiple diagnostic slides, we selected the primary tumor diagnostic slide with the largest tissue area, yielding 6,745 slides across 6,745 unique patients. Twelve additional TCGA cancer types were excluded because their dominant cell morphologies fall outside the training domain of the cell detection model (Supplementary Table 3).

Matched clinical data (overall survival, disease-specific survival, disease-free survival, and progression-free survival; age at diagnosis, sex, pathologic stage, tissue source site [TSS], and tumor purity estimates) were obtained from the TCGA Pan-Cancer Clinical Data Resource (TCGA-

CDR) (59). Molecular data included RNA-seq gene expression (RSEM normalized), somatic mutations from the MC3 multi-caller ensemble (61), copy-number variation, immune cell fraction estimates from CIBERSORT (62) and xCell (63), tumor purity from ABSOLUTE (64), and immune subtype classifications (C1–C6) from Thorsson et al. (10). All molecular data were retrieved from the GDC and PanCancerAtlas data repositories. Molecular data were matched to slides by TCGA case barcode (first 12 characters of the barcode); for cases with multiple aliquots, the primary tumor aliquot was selected. Thorsson immune subtype labels (C1–C6) were matched to slides by TCGA case barcode. Of 6,745 slides, 5,590 (82.9%) had matched immune subtype data; C5 (immunologically quiet, $n = 65$) and C6 (TGF- β dominant, $n = 27$) were retained but had limited statistical power.

4.2 Feature extraction

We computed 38 quantitative histological-morphometric (hereafter “histomic”) features per slide, organized into five categories: tissue composition (3 features), cell densities (6), nuclear morphology and kinetics (8), spatial organization (18), and spatial heterogeneity (3). Complete definitions, units, and category assignments are provided in Supplementary Table 1.

Feature extraction used two segmentation stages. Tissue segmentation used a CellViT-inspired architecture (65) with a Phikon self-supervised ViT-B backbone (66), trained on the PanopTILs crowdsourced annotation dataset (67); model weights are available in the code repository. We performed inference at 0.5 $\mu\text{m}/\text{px}$ on 224×224 pixel tiles with 32-pixel overlap; the final segmentation mask was obtained by majority voting in overlap regions. The model classified each tile into nine tissue classes: cancerous epithelium, stroma, necrosis, normal epithelium, TILs, junk/debris, blood, other, and whitespace (mean intersection-over-union = 0.72 on the PanopTILs held-out test set; note that per-class IoU varied substantially, and necrosis and normal epithelium had near-zero recall in deployment, reflecting their rarity in the training set and in resected TCGA specimens). Following the International Immuno-Oncology Biomarker Working Group recommendation (39), regions classified as TILs were reclassified as stroma before all downstream computation, yielding five effective compartments: cancerous epithelium, stroma, necrosis, normal epithelium, and blood.

Cell segmentation and classification used the HistoPLUS model (33), which detects and classifies individual cells into nine morphological types: tumor cells, lymphocytes, fibroblasts, plasmocytes, neutrophils, eosinophils, red blood cells, apoptotic bodies, and mitotic figures (mean panoptic quality [PQ] = 0.509 across cell types; per-class PQ varied from 0.28 to 0.73, with lowest performance on rare cell types such as eosinophils and apoptotic bodies). Inference was performed on 224×224 pixel tiles at $40\times$ magnification (0.25 $\mu\text{m}/\text{px}$) when available, falling back to $20\times$ (0.50 $\mu\text{m}/\text{px}$); the majority of slides were scanned at $40\times$. We extracted tiles with

a 64-pixel (16 μm) overlap margin; cells detected in overlap regions were deduplicated via a union-find algorithm that merges instances whose centroids fall within 10 μm , corresponding approximately to the diameter of a typical epithelial nucleus. The cell model was trained on pathologist annotations from eight cancer types (LUAD, LUSC, BRCA, COAD, BLCA, OV, PAAD, MESO); the remaining 13 included cancer types were processed in an out-of-distribution (OOD) setting. Tissue–cell discordance (cells in a tissue-model tumor region not classified as cancer cells by the cell model) varied from 0% to 12% across all cancer types, with the highest rate in PAAD (12.2%) despite being in-distribution, likely due to the dense desmoplastic stroma and small tumor glands characteristic of pancreatic ductal adenocarcinoma. OOD cancer types showed additional issues, including inflated kinetic indices in PRAD, LIHC, and THCA attributable to reduced cell-detection sensitivity. Red blood cells and plasmocytes were not used in feature computation.

All spatial features were computed on compartment masks resampled to a common resolution of $r = 8 \mu\text{m}/\text{px}$ by nearest-neighbor interpolation to ensure scanner-invariant boundary computation. Connected components below $A_{\min} = 2,048 \mu\text{m}^2$ (≈ 32 pixels at 8 $\mu\text{m}/\text{px}$, equivalent to approximately 5×5 cell diameters) were removed per compartment before distance transform computation to prevent noisy segmentation fragments from inflating boundary lengths. Five spatial bands were defined using the signed Euclidean distance transform d_T from the tumor boundary, where the tumor boundary was defined as the outer contour of the cancerous epithelium compartment mask at 8 $\mu\text{m}/\text{px}$ resolution (positive inside tumor, negative outside): tumor front B_T^{0-50} ($0 \leq d_T \leq 50 \mu\text{m}$), tumor core $B_T^{>50}$ ($d_T > 50 \mu\text{m}$), stroma near B_S^{0-50} ($-50 \leq d_T < 0$), stroma far B_S^{50-200} ($-200 \leq d_T < -50$), and necrosis ring R_{Nec}^{0-100} (within 100 μm of the necrosis boundary). The 50 μm front band corresponds to approximately five cell diameters; the 200 μm stroma cutoff was chosen as a heuristic approximation of the attenuation range of immune infiltration gradients, informed by spatial immune profiling studies (14, 68). We classified slides into growth-pattern regimes based on the tumor front fraction $\varphi = A(B_T^{0-50})/A(\Omega_T)$: mass-forming ($\varphi \leq 0.5$), intermediate ($0.5 < \varphi \leq 0.8$), or infiltrative ($\varphi > 0.8$). A macro-tumor mask obtained by morphological closing (disk radius $\rho = 200 \mu\text{m}$), used solely for computing the `micro_interface_ratio` QC metric, detected micro-interface dominance in infiltrative tumors.

Two additional features (normal epithelium area fraction and tumor–normal contact fraction, both dependent on normal epithelium detection, which the tissue model did not reliably identify) were excluded from the atlas entirely due to zero signal across all slides. Seven ratio features were susceptible to gate-loophole artifacts producing extreme values when denominators approached zero; these were mitigated by the winsorization step described below. Distance-based features (nearest-neighbor distances) were quantized at 8 $\mu\text{m}/\text{px}$ resolution owing to the tile grid spacing.

4.3 Feature preprocessing

Preprocessing of the 38 histomic features proceeded in three steps. First, 22 features with heavy right-skew (all cell densities, ratio features, distance features, and heterogeneity measures including coefficients of variation) were log-transformed using $\log(1+x)$. Second, all 38 features were winsorized at the 0.5th and 99.5th percentiles (computed per feature across the full cohort) to mitigate the influence of extreme values arising from segmentation artifacts. Global (pan-cohort) percentiles were used because the target artifacts (segmentation failures and ratio instabilities) are present across cancer types, though at varying rates (tissue–cell discordance ranges from 0% to 12% by cancer type). Per-cancer-type winsorization was not used because the small sample sizes of several cohorts (e.g., CHOL, $n = 38$) would yield unreliable percentile estimates. Third, features were z -score standardized to zero mean and unit variance. The scope of standardization varied by analysis: UMAP embeddings and K -means clustering used global z -scores (across all n samples), Cox regression used per-cancer-type z -scores (so hazard ratios reflect per-SD effects within each cancer type), and Spearman correlations used no z -score standardization (rank-based). Missing values (<2% of entries across all features) were imputed with the column median prior to standardization. Raw (untransformed) values were retained for display in the web atlas interface; all statistical models and embeddings consumed preprocessed values.

4.4 Survival analysis

We assessed associations between each histomic feature and four survival endpoints (overall survival [OS; designated as the primary endpoint], disease-specific survival [DSS], disease-free survival [DFS], and progression-free survival [PFS]) using univariate Cox proportional hazards (PH) regression, implemented with the `lifelines` Python package (69) (no L2 penalization; `penalizer=0.0`). Each model tests a single histomic feature (plus covariates); multivariate models incorporating multiple features simultaneously are not included in the current atlas (see Discussion). For each feature–cancer type–endpoint combination, we fitted two models: (1) unadjusted (feature only); and (2) adjusted (feature + age at diagnosis + sex + pathologic stage as covariates, stratified by tissue source site [TSS]). TSS was handled as a stratification variable in Cox models (`strata=['tss']` in `lifelines`), allowing each site to have its own baseline hazard function without consuming degrees of freedom, the standard approach for multi-center studies (70). Hazard ratios (HR) were reported per one standard deviation increase in the preprocessed feature value, with 95% Wald confidence intervals computed as $\exp(\hat{\beta}_1 \pm \Phi^{-1}(0.975) \cdot \text{SE}(\hat{\beta}_1))$, where SE was derived from the observed Fisher information matrix. Pan-cancer analyses used stratified Cox regression with cancer type as an additional stratification variable (`strata=['cancer_type']` in `lifelines`), allowing each cancer type its own baseline

hazard function while estimating a single shared regression coefficient. This approach avoids confounding by differential baseline hazard rates across cancer types. Per-cancer-type results constitute the primary analyses. Features and age were standardized (z -scored) prior to fitting; categorical covariates (sex, stage) were one-hot encoded with the first category dropped. For the adjusted model, we used multiple imputation by chained equations (MICE) with a Bayesian ridge regression imputer (`scikit-learn IterativeImputer`, 5 imputations, max 10 iterations per imputation, random seed incremented per imputation). Results were pooled using Rubin’s rules, yielding combined hazard ratios, standard errors, and P -values; the fraction of missing information (FMI) was recorded for each analysis. When covariate missingness exceeded 20% in any variable, when total sample size was below 30, or when fewer than 3 of 5 imputations produced valid fits, MICE was skipped and complete-case analysis was used as a fallback. Missingness arose primarily from incomplete staging annotations and varied by cancer type (Supplementary Table 8). A minimum sample size of $n \geq 30$ with ≥ 10 events was required per feature–cancer type–endpoint combination. Models were fitted only when the residual degrees of freedom remained positive after accounting for all covariates.

We tested the proportional hazards assumption for every fitted model using Schoenfeld residuals with the Kaplan–Meier time transform (71). The PH test P -value was used to flag each association: “pass” ($P \geq 0.05$), “warn” ($0.01 \leq P < 0.05$), or “fail” ($P < 0.01$). The $P < 0.01$ threshold for failure was chosen to balance sensitivity against the high multiple-testing burden (hundreds of models per cancer type); we note that this threshold has asymmetric power: large cohorts (e.g., BRCA, $n \approx 960$) can detect trivial PH departures, whereas small cohorts (e.g., CHOL, $n = 36$) have limited power to detect even substantial violations. The prevalence of PH violations across cancer types and endpoints is reported in Supplementary Table 7. When the PH assumption was violated ($P < 0.05$, encompassing both “warn” [$0.01 \leq P < 0.05$] and “fail” [$P < 0.01$] tiers), we invalidated the Cox hazard ratio, confidence intervals, and P -value (set to NaN), as these quantities are unreliable under non-proportional hazards. For BH correction, invalidated P -values were set to 1.0 to preserve the correction family size without inflating false discoveries. As a complementary, assumption-free summary, we additionally computed the restricted mean survival time (RMST) difference.

RMST was calculated as the area under the Kaplan–Meier curve up to a cancer-type-specific time horizon, with standard errors estimated using the Irwin variance formula (72). The default horizon was 1,095 days (3 years). For aggressive cancer types with short median survival, we used a 2-year horizon (PAAD, MESO). For indolent cancer types, we used a 5-year horizon (THCA, PRAD). These horizons were chosen to ensure adequate follow-up and at-risk populations at the truncation point; cancer-type-specific values are listed in Supplementary Table 9. RMST differences between high and low

feature groups (median split) were tested using a permutation procedure (5,000 permutations of group labels). The median split was used for interpretability and consistency with the clinical convention of risk stratification; we acknowledge that dichotomization discards information and reduces statistical power relative to continuous methods (73). P -values were computed as $P = (\#\{b : |\Delta_b| \geq |\Delta^{\text{obs}}|\} + 1)/(B + 1)$. Bootstrap confidence intervals (95%) for the RMST difference were obtained from 1,000 bootstrap resamples of the full cohort, using the percentile method. RMST analyses required $n \geq 20$ total subjects with ≥ 5 observations per group.

For cluster-level survival comparisons, a two-sided log-rank test was computed between cluster members and non-members, with BH correction applied within each combination of cluster level, analysis type, cancer type, and endpoint.

4.5 Molecular correlations

We computed Spearman rank correlations between each of the 38 histomic features and 293 molecular targets: 133 curated genes drawn from established cancer gene panels (OncoKB (74), COSMIC Cancer Gene Census (75)), immune checkpoint targets (TIGIT, PD-L1, CTLA4, LAG3), and EMT/stemness markers curated from Nieto et al. (42) (complete list in Supplementary Table 4), each assessed for both expression and copy-number variation ($133 \times 2 = 266$); 21 MSigDB Hallmark pathway scores (34) (of the 50 Hallmark gene sets [Supplementary Table 5], 21 had sufficient matched data after intersection filtering); and 6 immune cell fraction scores from CIBERSORT (62). Pathway activity scores were computed via single-sample Gene Set Enrichment Analysis (ssGSEA; gseapy 1.1.12) (76) using the full TCGA Pan-Cancer batch-corrected RNA-seq expression matrix ($\sim 20,500$ genes per sample, EB++AdjustPANCAN_IlluminaHiSeq_RNASeqV2 from UCSC Xena (77)). The 50 Hallmark gene sets (median ~ 200 genes per pathway) provide well-characterized, non-redundant representations of biological processes with established provenance (34). Gene sets with fewer than 10 genes present in the expression matrix after intersection were excluded (a stricter threshold than GSEA enrichment analysis below, because per-sample ssGSEA scores are noisier with small gene sets).

For unadjusted models, we computed the standard Spearman correlation coefficient and its analytical P -value (t -approximation) using `scipy.stats.spearmanr`, which is accurate for $n \geq 10$ and avoids the P -value banding that occurs with permutation floors. Bootstrap confidence intervals (95%) were obtained from 1,000 resamples using the percentile method: for each resample, observations were drawn with replacement, ranks recomputed, and the Spearman ρ recorded.

For covariate-adjusted models, we computed partial Spearman correlations via the following procedure: (1) rank-transform both the histomic feature and the molecular target, as well as all covariates; (2) residualize the ranked

feature and ranked target against the ranked covariates using ordinary least-squares regression; and (3) compute the Pearson correlation of the residuals, yielding the partial Spearman ρ (78). P -values for partial correlations were obtained using the standard t -test for partial correlations: $t = r\sqrt{\text{df}/(1-r^2)}$ with $\text{df} = n - 2 - k$, where k is the number of covariate columns after one-hot encoding, and a two-sided P -value from the $t(\text{df})$ distribution. This matches the approach used by R’s `ppcor::pcor.test()` and Python’s `pingouin.partial_corr()`. Bootstrap CIs for the partial Spearman ρ were obtained from 1,000 resamples, each recomputing the full rank-residualize-correlate pipeline.

A cancer type was included in the correlation analysis if it contained $n \geq 30$ samples; individual feature pairs required $n \geq 10$ non-missing observations. All correlations were computed per cancer type. Deterministic per-task random seeds were derived from a hash of the cancer type, histomic feature, and molecular feature names, ensuring reproducibility across parallel executions.

In total, the correlation analysis comprised 487,638 histomic-molecular pairs: 38 features \times 293 molecular targets (133 genes \times 2 data types [expression and copy number] + 21 Hallmark pathway scores + 6 immune cell scores) \times 22 cohorts (21 cancer types + pan-cancer), each evaluated under two adjustment models (unadjusted and adjusted [age, sex, stage, TSS]); the stated total excludes combinations with insufficient data. TSS was included as a grouped covariate rather than a stratification variable because the rank-residualization procedure requires explicit covariate columns; TSS was grouped into the five most frequent sites per cancer type, with remaining sites collapsed to “Other”, to limit the number of dummy variables in the residualization.

4.6 Categorical associations

Associations between histomic features and categorical molecular variables (somatic mutations [mutant vs. wild-type], copy-number alterations [amplification/deletion vs. neutral], and immune subtypes [C1–C6]) were tested separately for each cancer type.

For unadjusted models, inference used the exact or asymptotic distribution of the test statistic as implemented in `scipy.stats`. Two-group comparisons used the Mann-Whitney U test (two-sided) with Cliff’s δ as the effect size. Cliff’s δ was computed as the mean of the sign matrix $\text{sign}(x_i - y_j)$ over all $n_1 \times n_2$ pairs, with 95% bootstrap CIs (1,000 resamples); bootstrap rather than analytical CIs were used because the data contain tied values, which violate the continuity assumption of Cliff’s analytical variance formula (79). For variables with more than two levels, we used the Kruskal-Wallis H test with $\eta_H^2 = (H - k + 1)/(N - k)$ as the effect size (80), floored at zero. Bootstrap CIs for η^2 were obtained from 1,000 resamples of the group arrays.

For covariate-adjusted models, we used rank-ANCOVA with Freedman-Lane permutation inference (81). The response (histomic feature) and all covariates were rank-

transformed. The group effect was tested by comparing the full model (group dummies + rank-transformed covariates) to the reduced model (covariates only) via an F -statistic on the residual sum of squares. P -values were obtained by permuting residuals from the covariate-only model (1,000 permutations). The F -statistic null distribution is parametrically smooth (approximately F -distributed under the null), requiring relatively few permutations for stable P -value estimation; with 1,000 permutations the minimum achievable P -value is ≈ 0.001 , sufficient for BH correction within the per-cancer-type families used here. The effect size was partial $\eta^2 = SS_{\text{group}} / (SS_{\text{group}} + SS_{\text{residual}})$. Bootstrap CIs for partial η^2 were computed from 1,000 resamples.

Group ordering for binary comparisons followed a deterministic convention: mutant before wild-type, amplification/deletion before neutral. This ensured consistent sign interpretation of Cliff’s δ across analyses. A minimum of $n \geq 30$ total observations and ≥ 5 observations per group was required; groups smaller than 5 were excluded.

4.7 Clustering

Unsupervised morphological clustering was performed in two tiers. At the L1 (pan-cancer) level, all 6,745 slides were clustered on the full 38-dimensional preprocessed feature vector (after log-transform, winsorization, and z -scoring). At the L2 (cancer-specific) level, clustering was performed independently within each cancer type using cancer-type-specific z -scores.

We used K -means clustering (`scikit-learn`, $n_{\text{init}} = 10$, random state fixed at 42). For L1, clustering was computed for $K \in \{3, \dots, 25\}$; silhouette, Calinski–Harabasz, Davies–Bouldin, and gap statistic scores were computed for each K . $K = 10$ was selected based on convergence of silhouette (local maximum at $K = 10$), Calinski–Harabasz (plateau), Davies–Bouldin (local minimum), and gap statistic scores, balancing cluster interpretability against granularity (the gap statistic favored $K = 8$; silhouette favored $K = 10$). K -means was chosen for its scalability and interpretability; the resulting clusters should be understood as a convenient partition of feature space rather than a claim about the true number of distinct morphological subtypes. We did not apply PCA dimensionality reduction before clustering; the 38-dimensional feature space was used directly to preserve interpretability of cluster feature profiles. The effective dimensionality (17 components explain 90% of variance) suggests moderate redundancy, which gives correlated features proportionally more weight. For L2, the number of clusters was selected by the elbow method: we computed inertia for K values ranging from 2 to 8 (depending on cohort size) and selected the K that maximized the perpendicular distance from each point to the line connecting the first and last ($K, \text{inertia}$) points in the normalized space (82). Cancer types with fewer than 20 samples were assigned a single cluster without optimization. For cancer types with ≥ 20 samples, this yielded $K \in [2, 7]$ (69 L2 subclusters total). Individual clusters with fewer than 10

samples were excluded. Internal validation metrics (silhouette score, Calinski–Harabasz index, and Davies–Bouldin index) were computed for each candidate K and reported alongside the selected solution.

Cluster stability was assessed via repeated random subsampling: 50 iterations of 80% subsampling without replacement, re-clustering with the same K and $n_{\text{init}} = 10$, and comparison to the original labels using the adjusted Rand index (ARI) and mean best-match Jaccard index across clusters (83). The 50-iteration count provides sufficient precision for stability estimation: at $\text{ARI} = 0.72$, the Monte Carlo standard error is ≈ 0.02 , small relative to the typical gap between stable and unstable solutions. Cluster names were automatically generated from a structured schema. Each cluster received an immune axis label (immune-hot, immune-cold, or immune-mixed, based on mean z -score > 0.5 or < -0.5 across five immune features), a stromal axis label (stroma-high, stroma-low, or stroma-mid), the label of the most extreme non-immune, non-stromal feature, and a cancer-enrichment tag when a single cancer type constituted $\geq 40\%$ of the cluster.

Two-dimensional visualization was performed using UMAP (uniform manifold approximation and projection) with $n_{\text{neighbors}} = 15$, $\text{min_dist} = 0.1$, Euclidean metric, and random state 42, applied to the z -scored feature matrix after median imputation of missing values (84). UMAP was used for visualization only; no statistical inference was drawn from the embedding coordinates, and all clustering was performed in the original 38-dimensional feature space, so UMAP hyperparameter sensitivity does not affect statistical conclusions.

4.8 Cluster enrichment

Mutation enrichment. Mutation enrichment for each cluster was tested using Fisher’s exact test on 2×2 contingency tables (mutated vs. wild-type \times in-cluster vs. out-of-cluster), with odds ratios (OR) and exact 95% confidence intervals. Fisher’s exact test conditions on both margins and is therefore conservative when only the row margin (cluster membership) is fixed; we accepted this conservatism in exchange for exact P -values without distributional assumptions. A minimum of 20 total observations and 5 mutated samples were required per test.

Pathway enrichment. Pathway enrichment was assessed using two complementary approaches. First, for each cluster, we compared the distribution of pathway activity scores (in-cluster vs. out-of-cluster) using the Mann–Whitney U test with Cliff’s δ as the effect size and 1,000-resample bootstrap CIs. Second, we performed gene set enrichment analysis (GSEA) (85) with phenotype permutation. Gene-level t -statistics were computed from Welch’s t -test comparing in-cluster to out-of-cluster expression. The enrichment score (ES) was calculated as the weighted running sum statistic using absolute t -statistics as weights. Significance was assessed

by permuting sample phenotype labels (1,000 permutations). P -values were computed separately for positive and negative enrichment:

$$P = \begin{cases} (\#\{b : ES_b^+ \geq ES^{\text{obs}}\} + 1) / (\#\{ES_b^+\} + 1) & \text{if } ES^{\text{obs}} > 0, \\ (\#\{b : ES_b^- \leq ES^{\text{obs}}\} + 1) / (\#\{ES_b^-\} + 1) & \text{if } ES^{\text{obs}} < 0, \end{cases}$$

where ES_b^+ and ES_b^- denote the positive and negative tails of the null distribution, respectively. Normalized enrichment scores (NES) were obtained by dividing the observed ES by the mean of the positive or negative tail of the null distribution. False discovery rates (FDR q -values) were computed using the pooled null NES distribution across all gene sets, following the standard GSEA procedure (85). Gene sets with FDR $q < 0.25$ were considered significant. The FDR $q < 0.25$ threshold follows the original GSEA convention (85), reflecting the exploratory nature of pathway enrichment and the lower statistical power of rank-based enrichment relative to parametric tests used elsewhere. Leading-edge genes (up to 20 per pathway) were recorded. Gene sets with fewer than 3 genes present in the expression matrix after intersection were excluded.

Immune subtype enrichment. Immune subtype enrichment (Thorsson C1–C6 classification) was tested per cluster using Fisher’s exact test on 2×2 tables (subtype present/absent \times in-cluster/out-of-cluster), with odds ratios, exact 95% CIs, and observed-to-expected ratios.

4.9 Multiple testing correction

All P -values were corrected for multiple comparisons using the Benjamini–Hochberg (BH) procedure (46) applied within explicitly defined correction families. Each family was defined to group biologically coherent tests while avoiding excessive conservatism from pooling unrelated analyses (Supplementary Table 6 lists the exact family definition for each analysis type). For example, survival correction families were defined per cancer type \times endpoint \times adjustment model, ensuring that BH correction pools only the 38 feature-level tests within a single biological context. GSEA used its own canonical FDR procedure based on pooled null NES distributions rather than BH correction (85). Every adjusted P -value was stored alongside the correction family identifier and the number of tests in the family (`correction_family_id, n_tests_in_family`) to enable post hoc verification.

OS was designated as the primary survival endpoint; DSS, DFS, and PFS are reported as sensitivity analyses. BH correction was applied independently per endpoint rather than pooling across endpoints, which is appropriate because the endpoints have partially overlapping event definitions (OS and DSS share events) and thus violate the independence assumption of joint correction. Cross-endpoint replication (i.e., the fraction of OS-significant associations that also reach significance for DSS or PFS) is reported as an informal consistency check rather than a formal multiplicity-controlled comparison.

Statistical conventions. Permutation P -values (RMST, rank-ANCOVA) used the add-one correction of Phipson and Smyth (86): $P = (B^+ + 1) / (B + 1)$. Bootstrap confidence intervals (1,000 resamples, percentile method) were computed for all effect sizes; CIs were reported only when $\geq 90\%$ of resamples produced valid estimates (a resample was invalid when zero-variance columns or singular covariate matrices prevented model fitting). One thousand resamples provide adequate precision for central tendency estimation (Monte Carlo SE < 0.01 for moderate effect sizes); tail coverage may be imprecise for extreme quantiles. Permutation counts were set to 5,000 for RMST (where permutation is the sole inference method), 1,000 for GSEA (with 1,000 permutations the minimum achievable P -value is ≈ 0.001 , sufficient for the BH correction applied within per-cluster families), and 1,000 for rank-ANCOVA (where the F -statistic null distribution is approximately parametric, yielding stable P -value estimates with fewer permutations). Minimum sample sizes were set based on the number of parameters estimated: $n \geq 30$ for regression models with covariates (Cox, Spearman, rank-ANCOVA), $n \geq 20$ for nonparametric group comparisons (RMST, Fisher’s exact test). Ties were handled using midranking for Spearman correlations and the normal approximation with continuity correction for Mann–Whitney U tests, as implemented in `scipy.stats`. Throughout the text, statistical significance refers to $P_{\text{adj}} < 0.05$ (BH-corrected) unless otherwise stated.

4.10 Batch effect assessment

We assessed potential batch effects from tissue source site (TSS) using two complementary approaches. Principal variance component analysis (PVCA) (47) decomposed variance in the top principal components (selected to explain $\geq 80\%$ cumulative variance, up to 10 components) into TSS (batch), cancer type (biological), and residual fractions using marginal one-way ANOVA η^2 for each factor (TSS, cancer type) applied independently to each principal component, weighted by explained variance ratio. Because TSS and cancer type are not orthogonal (most sites contribute predominantly one cancer type), the marginal η^2 values can sum to more than 1.0 per component; residual variance was computed as $\max(0, 1 - \eta_{\text{batch}}^2 - \eta_{\text{bio}}^2)$ and all three fractions were renormalized to sum to 1.0. Feature matrices were standardized prior to PCA. PVCA was computed both globally (all slides) and per cancer type (TSS variance within each cancer type).

Silhouette analysis treated TSS labels as cluster assignments and computed the mean silhouette score on standardized features (Euclidean distance), with subsampling to 5,000 slides for computational efficiency. A silhouette score near zero or negative indicated minimal TSS-driven clustering. Scores above 0.25 were flagged as moderate batch effects, and scores above 0.5 as strong batch effects. Per-batch mean silhouette scores identified specific sites with anomalous feature distributions. We visually inspected UMAP embeddings

colored by TSS to confirm that slides did not cluster by source site after controlling for cancer type.

4.11 Power analysis and evidence badges

We computed the minimum detectable effect size (MDES) at 80% power ($\alpha = 0.05$, two-sided) for every analysis to characterize the sensitivity limits of each cancer-type cohort. For survival associations, MDES used the Schoenfeld–Freedman approximation (48, 49); for correlations, the Fisher z -transform; for categorical associations, simulation-based power curves (2,000 simulated datasets with binary-search convergence). Formulas are provided in Supplementary Methods.

Every association in the atlas was assigned an evidence-strength badge: **strong** ($P_{\text{adj}} < 0.01$, effect size above threshold, narrow CI, $n \geq 100$), **moderate** ($P_{\text{adj}} < 0.05$, effect size above threshold, narrow or moderate CI, $n \geq 50$), **suggestive** ($P_{\text{adj}} < 0.10$ or CI excludes null [$\text{HR} = 1$, $\rho = 0$, $\delta = 0$, or $\eta^2 = 0$], $n \geq 30$), or **insufficient** ($n < 30$ or missing statistics). Effect-size thresholds were set at two tiers guided by conventional benchmarks (87). **Strong** thresholds (Cohen’s medium): $\text{HR} \geq 1.5$ (or ≤ 0.667), $|\rho| \geq 0.3$, $|\text{Cliff’s } \delta| \geq 0.3$, $\eta^2 \geq 0.06$. **Moderate** thresholds (Cohen’s small): $\text{HR} \geq 1.18$ (or ≤ 0.847), $|\rho| \geq 0.1$, $|\text{Cliff’s } \delta| \geq 0.15$, $\eta^2 \geq 0.01$. CI width was categorized as “narrow” (ratio CI $< 2\times$; additive CI width < 0.3), “moderate” ($< 4\times$; < 0.6), or “wide” (otherwise). Sample size thresholds were $n \geq 100$ for strong, $n \geq 50$ for moderate, and $n < 30$ for insufficient evidence.

4.12 Web application

The HistoAtlas web atlas is built using Astro (static site generator) with React interactive components. All precomputed statistical results, feature profiles, cluster metadata, and visualization data are serialized as static JSON files during the build process. No backend computation server is required at runtime, enabling deployment on static hosting infrastructure. The interface provides pan-cancer and per-cancer views of UMAP embeddings, feature distributions, survival associations, molecular correlations, and cluster profiles. Users can filter by cancer type, feature category, evidence badge, and statistical significance.

Spatial interpretability. The interface provides three complementary visualization layers. First, a tissue compartment map displays a spatial segmentation overlay per slide showing five tissue compartments mapped to nine spatial zones (tumor front, tumor core, peritumoral stroma at three distance bands [0–50 μm , 50–200 μm , >200 μm], necrosis ring, necrosis, normal epithelium, and background), enabling users to identify any pixel’s anatomical region by hovering (Fig. 6a). Second, for each of the 38 histomic features, the interface displays the top-5 ranked 224×224 pixel tiles from the slide, scored by the feature’s computation strategy. Each tile includes exact pixel coordinates on the whole-slide image, a 10 μm scale bar,

and a toggleable cell-type prediction overlay showing 14 cell types in distinct colors (Fig. 6c,d). Third, bidirectional navigation links statistical results to the slides and tissue regions that generated them: from survival hazard ratios and molecular correlations to feature pages, and from feature pages to specific tiles on specific slides.

4.13 Implementation and reproducibility

All analyses were implemented in Python 3.11 and orchestrated by a Snakemake workflow (88) that defines a directed acyclic graph of computational dependencies.

Key library versions: lifelines 0.29.0, scipy 1.12.0, scikit-learn 1.4.0, umap-learn 0.5.5, gseapy 1.1.12, statsmodels 0.14.1, numpy 1.26.4, pandas 2.2.0. All random processes (permutation tests, bootstrap resampling (effect-size CIs), subsampling (cluster stability), K -means initialization) used explicit random seeds.

Data and code availability. All analysis code, precomputed results, and the web application are available at <https://github.com/histoatlas/histoatlas>. The interactive atlas is accessible at <https://histoatlas.com> (RRID:SCR_028056). Derived feature matrices, precomputed statistical results, and model weights will be deposited in a public repository with a persistent DOI prior to publication. The GDC file UUIDs for all 6,745 slides used in this study are listed in the code repository.

References

- [1] Bera, K., Schalper, K. A., Rimm, D. L., Velcheti, V. & Madabhushi, A. Artificial intelligence in digital pathology — new tools for diagnosis and precision oncology. *Nature Reviews Clinical Oncology* **16**, 703–715 (2019).
- [2] Kather, J. N. *et al.* Pan-cancer image-based detection of clinically actionable genetic alterations. *Nature Cancer* **1**, 789–799 (2020).
- [3] Gurcan, M. N. *et al.* Histopathological image analysis: A review. *IEEE Reviews in Biomedical Engineering* **2**, 147–171 (2009).
- [4] van der Laak, J., Litjens, G. & Ciompi, F. Deep learning in histopathology: the path to the clinic. *Nature Medicine* **27**, 775–784 (2021).
- [5] Kandath, C. *et al.* Mutational landscape and significance across 12 major cancer types. *Nature* **502**, 333–339 (2013).
- [6] Hoadley, K. A. *et al.* Multiplatform analysis of 12 cancer types reveals molecular classification within and across tissues of origin. *Cell* **158**, 929–944 (2014).

- [7] Li, Y. *et al.* Proteogenomic data and resources for pan-cancer analysis. *Cancer Cell* **41**, 1397–1406 (2023).
- [8] Corces, M. R. *et al.* The chromatin accessibility landscape of primary human cancers. *Science* **362**, eaav1898 (2018).
- [9] Hoadley, K. A. *et al.* Cell-of-origin patterns dominate the molecular classification of 10,000 tumors from 33 types of cancer. *Cell* **173**, 291–304.e6 (2018).
- [10] Thorsson, V. *et al.* The immune landscape of cancer. *Immunity* **48**, 812–830.e14 (2018).
- [11] Galon, J. *et al.* Type, density, and location of immune cells within human colorectal tumors predict clinical outcome. *Science* **313**, 1960–1964 (2006).
- [12] Pagès, F. *et al.* International validation of the consensus Immunoscore for the classification of colon cancer: a prognostic and accuracy study. *The Lancet* **391**, 2128–2139 (2018).
- [13] Fridman, W. H., Pagès, F., Sautès-Fridman, C. & Galon, J. The immune contexture in human tumours: impact on clinical outcome. *Nature Reviews Cancer* **12**, 298–306 (2012).
- [14] Saltz, J. *et al.* Spatial organization and molecular correlation of tumor-infiltrating lymphocytes using deep learning on pathology images. *Cell Reports* **23**, 181–193.e7 (2018).
- [15] Beck, A. H. *et al.* Systematic analysis of breast cancer morphology uncovers stromal features associated with survival. *Science Translational Medicine* **3**, 108ra113 (2011).
- [16] Yu, K.-H. *et al.* Predicting non-small cell lung cancer prognosis by fully automated microscopic pathology image features. *Nature Communications* **7**, 12474 (2016).
- [17] Cooper, L. A. D. *et al.* Novel genotype-phenotype associations in human cancers enabled by advanced molecular platforms and computational analysis of whole slide images. *Laboratory Investigation* **95**, 366–376 (2015).
- [18] Echle, A. *et al.* Deep learning in cancer pathology: a new generation of clinical biomarkers. *British Journal of Cancer* **124**, 686–696 (2021).
- [19] Coudray, N. *et al.* Classification and mutation prediction from non-small cell lung cancer histopathology images using deep learning. *Nature Medicine* **24**, 1559–1567 (2018).
- [20] Bannier, P.-A. *et al.* AI allows pre-screening of FGFR3 mutational status using routine histology slides of muscle-invasive bladder cancer. *Nature Communications* **15**, 10914 (2024).
- [21] Kather, J. N. *et al.* Deep learning can predict microsatellite instability directly from histology in gastrointestinal cancer. *Nature Medicine* **25**, 1054–1056 (2019).
- [22] Saillard, C. *et al.* Validation of MSIntuit as an AI-based pre-screening tool for MSI detection from colorectal cancer histology slides. *Nature Communications* **14**, 6695 (2023).
- [23] Schmauch, B. *et al.* A deep learning model to predict RNA-Seq expression of tumours from whole slide images. *Nature Communications* **11**, 3877 (2020).
- [24] Kather, J. N. *et al.* Predicting survival from colorectal cancer histology slides using deep learning: A retrospective multicenter study. *PLOS Medicine* **16**, e1002730 (2019).
- [25] Chen, R. J. *et al.* Towards a general-purpose foundation model for computational pathology. *Nature Medicine* **30**, 850–862 (2024).
- [26] Vorontsov, E. *et al.* A foundation model for clinical-grade computational pathology and rare cancers detection. *Nature Medicine* **30**, 2924–2935 (2024).
- [27] Saillard, C. *et al.* H-optimus-0 (2024). URL <https://github.com/bioptimus/releases/tree/main/models/h-optimus/v0>.
- [28] Diao, J. A. *et al.* Human-interpretable image features derived from densely mapped cancer pathology slides predict diverse molecular phenotypes. *Nature Communications* **12**, 1613 (2021).
- [29] Abel, J. *et al.* AI powered quantification of nuclear morphology in cancers enables prediction of genome instability and prognosis. *npj Precision Oncology* **8**, 134 (2024).
- [30] Cerami, E. *et al.* The cBio cancer genomics portal: An open platform for exploring multidimensional cancer genomics data. *Cancer Discovery* **2**, 401–404 (2012).
- [31] Clark, K. *et al.* The Cancer Imaging Archive (TCIA): Maintaining and operating a public information repository. *Journal of Digital Imaging* **26**, 1045–1057 (2013).
- [32] Uhlén, M. *et al.* Tissue-based map of the human proteome. *Science* **347**, 1260419 (2015).
- [33] Adjadj, B. *et al.* Towards comprehensive cellular characterisation of H&E slides. *arXiv preprint* (2025). URL <https://arxiv.org/abs/2508.09926>. 2508.09926.
- [34] Liberzon, A. *et al.* The molecular signatures database (MSigDB) hallmark gene set collection. *Cell Systems* **1**, 417–425 (2015).

- [35] Radtke, F., MacDonald, H. R. & Tacchini-Cottier, F. Regulation of innate and adaptive immunity by Notch. *Nature Reviews Immunology* **13**, 427–437 (2013).
- [36] Radovich, M. *et al.* The integrated genomic landscape of thymic epithelial tumors. *Cancer Cell* **33**, 244–258.e10 (2018).
- [37] Cancer Genome Atlas Network. Comprehensive molecular characterization of human colon and rectal cancer. *Nature* **487**, 330–337 (2012).
- [38] Perou, C. M. *et al.* Molecular portraits of human breast tumours. *Nature* **406**, 747–752 (2000).
- [39] Salgado, R. *et al.* The evaluation of tumor-infiltrating lymphocytes (TILs) in breast cancer: recommendations by an International TILs Working Group 2014. *Annals of Oncology* **26**, 259–271 (2015).
- [40] Joyce, J. A. & Fearon, D. T. T cell exclusion, immune privilege, and the tumor microenvironment. *Science* **348**, 74–80 (2015).
- [41] Chen, D. S. & Mellman, I. Elements of cancer immunity and the cancer-immune set point. *Nature* **541**, 321–330 (2017).
- [42] Nieto, M. A., Huang, R. Y.-J., Jackson, R. A. & Thiery, J. P. EMT: 2016. *Cell* **166**, 21–45 (2016).
- [43] Elston, C. W. & Ellis, I. O. Pathological prognostic factors in breast cancer. I. The value of histological grade in breast cancer: experience from a large study with long-term follow-up. *Histopathology* **19**, 403–410 (1991).
- [44] Giese, A., Bjerkvig, R., Berens, M. E. & Westphal, M. Cost of migration: invasion of malignant gliomas and implications for treatment. *Journal of Clinical Oncology* **21**, 1624–1636 (2003).
- [45] Hatzikirou, H., Basanta, D., Simon, M., Schaller, K. & Deutsch, A. ‘Go-or-grow’: the key to the emergence of invasion in tumour biology. *Mathematical Medicine and Biology* **29**, 49–65 (2012).
- [46] Benjamini, Y. & Hochberg, Y. Controlling the false discovery rate: A practical and powerful approach to multiple testing. *Journal of the Royal Statistical Society: Series B (Methodological)* **57**, 289–300 (1995).
- [47] Li, J., Bushel, P. R., Chu, T.-M. & Wolfinger, R. D. Principal variance components analysis: Estimating batch effects in microarray gene expression data. In Scherer, A. (ed.) *Batch Effects and Noise in Microarray Experiments: Sources and Solutions*, 141–154 (John Wiley & Sons, 2009).
- [48] Schoenfeld, D. A. Sample-size formula for the proportional-hazards regression model. *Biometrics* **39**, 499–503 (1983).
- [49] Freedman, L. S. Tables of the number of patients required in clinical trials using the logrank test. *Statistics in Medicine* **1**, 121–129 (1982).
- [50] Loi, S. *et al.* Tumor-infiltrating lymphocytes and prognosis: A pooled individual patient analysis of early-stage triple-negative breast cancers. *Journal of Clinical Oncology* **37**, 559–569 (2019).
- [51] Denkert, C. *et al.* Tumour-infiltrating lymphocytes and prognosis in different subtypes of breast cancer: a pooled analysis of 3771 patients treated with neoadjuvant therapy. *The Lancet Oncology* **19**, 40–50 (2018).
- [52] Nigg, E. A. Mitotic kinases as regulators of cell division and its checkpoints. *Nature Reviews Molecular Cell Biology* **2**, 21–32 (2001).
- [53] Carretero, R. *et al.* Eosinophils orchestrate cancer rejection by normalizing tumor vessels and enhancing infiltration of CD8+ T cells. *Nature Immunology* **16**, 609–617 (2015).
- [54] Sahai, E. *et al.* A framework for advancing our understanding of cancer-associated fibroblasts. *Nature Reviews Cancer* **20**, 174–186 (2020).
- [55] Marusyk, A., Almendro, V. & Polyak, K. Intra-tumour heterogeneity: a looking glass for cancer? *Nature Reviews Cancer* **12**, 323–334 (2012).
- [56] Galon, J. & Bruni, D. Approaches to treat immune hot, altered and cold tumours with combination immunotherapies. *Nature Reviews Drug Discovery* **18**, 197–218 (2019).
- [57] Sautès-Fridman, C., Petitprez, F., Calderaro, J. & Fridman, W. H. Tertiary lymphoid structures in the era of cancer immunotherapy. *Nature Reviews Cancer* **19**, 307–325 (2019).
- [58] Uhlén, M. *et al.* A pathology atlas of the human cancer transcriptome. *Science* **357**, eaan2507 (2017).
- [59] Liu, J. *et al.* An integrated TCGA pan-cancer clinical data resource to drive high-quality survival outcome analytics. *Cell* **173**, 400–416.e11 (2018).
- [60] Curtis, C. *et al.* The genomic and transcriptomic architecture of 2,000 breast tumours reveals novel subgroups. *Nature* **486**, 346–352 (2012).
- [61] Ellrott, K. *et al.* Scalable open science approach for mutation calling of tumor exomes using multiple genomic pipelines. *Cell Systems* **6**, 271–281.e7 (2018).
- [62] Newman, A. M. *et al.* Robust enumeration of cell subsets from tissue expression profiles. *Nature Methods* **12**, 453–457 (2015).

- [63] Aran, D., Hu, Z. & Butte, A. J. xCell: digitally portraying the tissue cellular heterogeneity landscape. *Genome Biology* **18**, 220 (2017).
- [64] Carter, S. L. *et al.* Absolute quantification of somatic DNA alterations in human cancer. *Nature Biotechnology* **30**, 413–421 (2012).
- [65] Hörst, F. *et al.* CellViT: Vision transformers for precise cell segmentation and classification. *Medical Image Analysis* **94**, 103143 (2024).
- [66] Filiot, A. *et al.* Scaling self-supervised learning for histopathology with masked image modeling. *medRxiv* (2023).
- [67] Amgad, M., Salgado, R. & Cooper, L. A. D. A panoptic segmentation dataset for explainable scoring of tumor-infiltrating lymphocytes. *npj Breast Cancer* **10**, 66 (2024).
- [68] Keren, L. *et al.* A structured tumor-immune microenvironment in triple negative breast cancer revealed by multiplexed ion beam imaging. *Cell* **174**, 1373–1387.e19 (2018).
- [69] Davidson-Pilon, C. lifelines: survival analysis in Python. *Journal of Open Source Software* **4**, 1317 (2019).
- [70] Therneau, T. M. & Grambsch, P. M. *Modeling Survival Data: Extending the Cox Model* (Springer, 2000).
- [71] Grambsch, P. M. & Therneau, T. M. Proportional hazards tests and diagnostics based on weighted residuals. *Biometrika* **81**, 515–526 (1994).
- [72] Irwin, J. O. The standard error of an estimate of expectation of life, with special reference to expectation of tumourless life in experiments with mice. *Journal of Hygiene* **47**, 188–189 (1949).
- [73] Royston, P., Altman, D. G. & Sauerbrei, W. Dichotomizing continuous predictors in multiple regression: a bad idea. *Statistics in Medicine* **25**, 127–141 (2006).
- [74] Chakravarty, D. *et al.* OncoKB: A precision oncology knowledge base. *JCO Precision Oncology* **1**, 1–16 (2017).
- [75] Sondka, Z. *et al.* The COSMIC Cancer Gene Census: describing genetic dysfunction across all human cancers. *Nature Reviews Cancer* **18**, 696–705 (2018).
- [76] Barbie, D. A. *et al.* Systematic RNA interference reveals that oncogenic KRAS-driven cancers require TBK1. *Nature* **462**, 108–112 (2009).
- [77] Goldman, M. J. *et al.* Visualizing and interpreting cancer genomics data via the Xena platform. *Nature Biotechnology* **38**, 675–678 (2020).
- [78] Conover, W. J. *Practical Nonparametric Statistics* (John Wiley & Sons, 1999), 3rd edn.
- [79] Cliff, N. Dominance statistics: Ordinal analyses to answer ordinal questions. *Psychological Bulletin* **114**, 494–509 (1993).
- [80] Tomczak, M. & Tomczak, E. The need to report effect size estimates revisited. An overview of some recommended measures of effect size. *Trends in Sport Sciences* **21**, 19–25 (2014).
- [81] Freedman, D. & Lane, D. A nonstochastic interpretation of reported significance levels. *Journal of Business & Economic Statistics* **1**, 292–298 (1983).
- [82] Thorndike, R. L. Who belongs in the family? *Psychometrika* **18**, 267–276 (1953).
- [83] Hennig, C. Cluster-wise assessment of cluster stability. *Computational Statistics & Data Analysis* **52**, 258–271 (2007).
- [84] McInnes, L., Healy, J., Saul, N. & Großberger, L. UMAP: Uniform manifold approximation and projection for dimension reduction. *Journal of Open Source Software* **3**, 861 (2018).
- [85] Subramanian, A. *et al.* Gene set enrichment analysis: A knowledge-based approach for interpreting genome-wide expression profiles. *Proceedings of the National Academy of Sciences* **102**, 15545–15550 (2005).
- [86] Phipson, B. & Smyth, G. K. Permutation P-values should never be zero: Calculating exact P-values when permutations are randomly drawn. *Statistical Applications in Genetics and Molecular Biology* **9**, Article 39 (2010).
- [87] Chen, H., Cohen, P. & Chen, S. How big is a big odds ratio? Interpreting the magnitudes of odds ratios in epidemiological studies. *Communications in Statistics – Simulation and Computation* **39**, 860–864 (2010).
- [88] Mölder, F. *et al.* Sustainable data analysis with Snake-make. *F1000Research* **10**, 33 (2021).
- [89] Helmink, B. A. *et al.* B cells and tertiary lymphoid structures promote immunotherapy response. *Nature* **577**, 549–555 (2020).
- [90] Petitprez, F. *et al.* B cells are associated with survival and immunotherapy response in sarcoma. *Nature* **577**, 556–560 (2020).
- [91] Schürch, C. M. *et al.* Coordinated cellular neighborhoods orchestrate antitumoral immunity at the colorectal cancer invasive front. *Cell* **182**, 1341–1359.e19 (2020).
- [92] Aran, D., Sirota, M. & Butte, A. J. Systematic pan-cancer analysis of tumour purity. *Nature Communications* **6**, 8971 (2015).

- [93] Hänzelmann, S., Castelo, R. & Guinney, J. GSVA: gene set variation analysis for microarray and RNA-Seq data. *BMC Bioinformatics* **14**, 7 (2013).

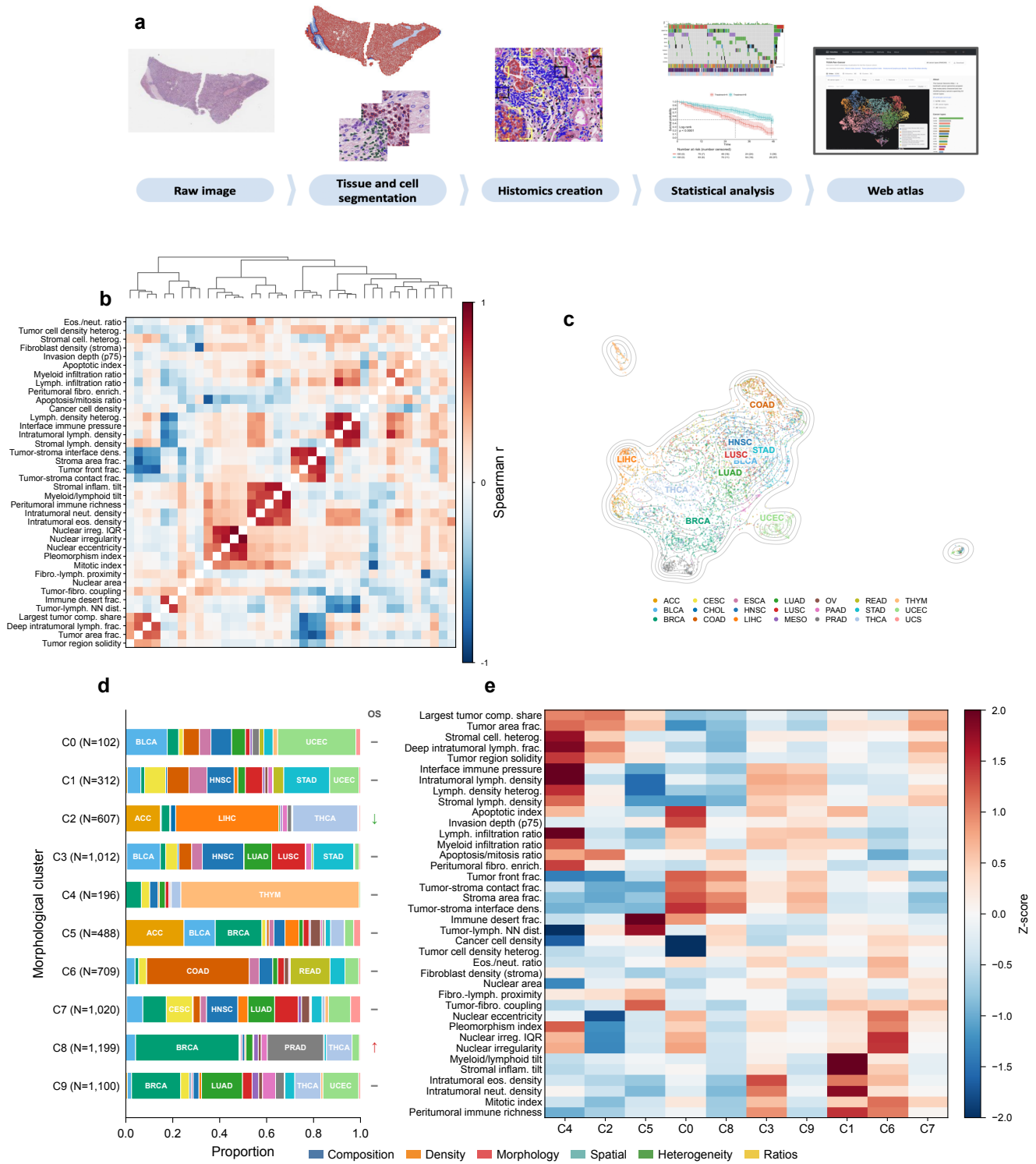


Figure 1: The HistoAtlas pipeline and pan-cancer morphological landscape. (a) Overview of the computational pipeline. Diagnostic H&E-stained whole-slide images (6,745 slides, 21 TCGA cancer types) are segmented into tissue compartments (tumor core, stroma, invasive front), followed by cell-level detection and classification of 9 cell types. From each slide, 38 quantitative histomic features are extracted spanning tissue composition, cell densities, nuclear morphology, spatial immune topology, microenvironment heterogeneity, and cell-type ratios. (b) Pairwise Spearman correlation matrix of the 38 features computed across all 6,745 slides. Ward-linkage hierarchical clustering reveals structured modules: density features form a tight positive-correlation block, morphology features cluster together, and cross-module anti-correlations delineate distinct biological axes. Left color bar indicates feature category. Diagonal entries are masked. (c) UMAP embedding of all 6,745 slides colored by cancer type. Cancer types with distinct morphological programs (e.g., THYM, THCA) occupy separated regions, while adenocarcinomas (BRCA, LUAD, STAD) partially overlap. Gray contour lines indicate point density. (d) Cancer type composition of each L1 morphological cluster ($K = 10$, horizontal stacked bars), with cluster sizes indicated at left. Cancer types constituting more than 10% of a cluster are labeled within the bar. Right annotation shows overall survival direction per cluster (green arrow: significantly protective, $HR < 1$; red arrow: significantly adverse, $HR > 1$; gray dash: non-significant). (e) Heatmap of z-scored mean feature values per cluster, with Ward-linkage hierarchical clustering applied to both features (rows) and clusters (columns). Feature labels are colored by category. Red indicates elevated values; blue indicates suppressed values relative to the pan-cancer mean. Values are clipped at $z = \pm 2$ for visualization. $N = 6,745$ slides from 21 TCGA cancer types.

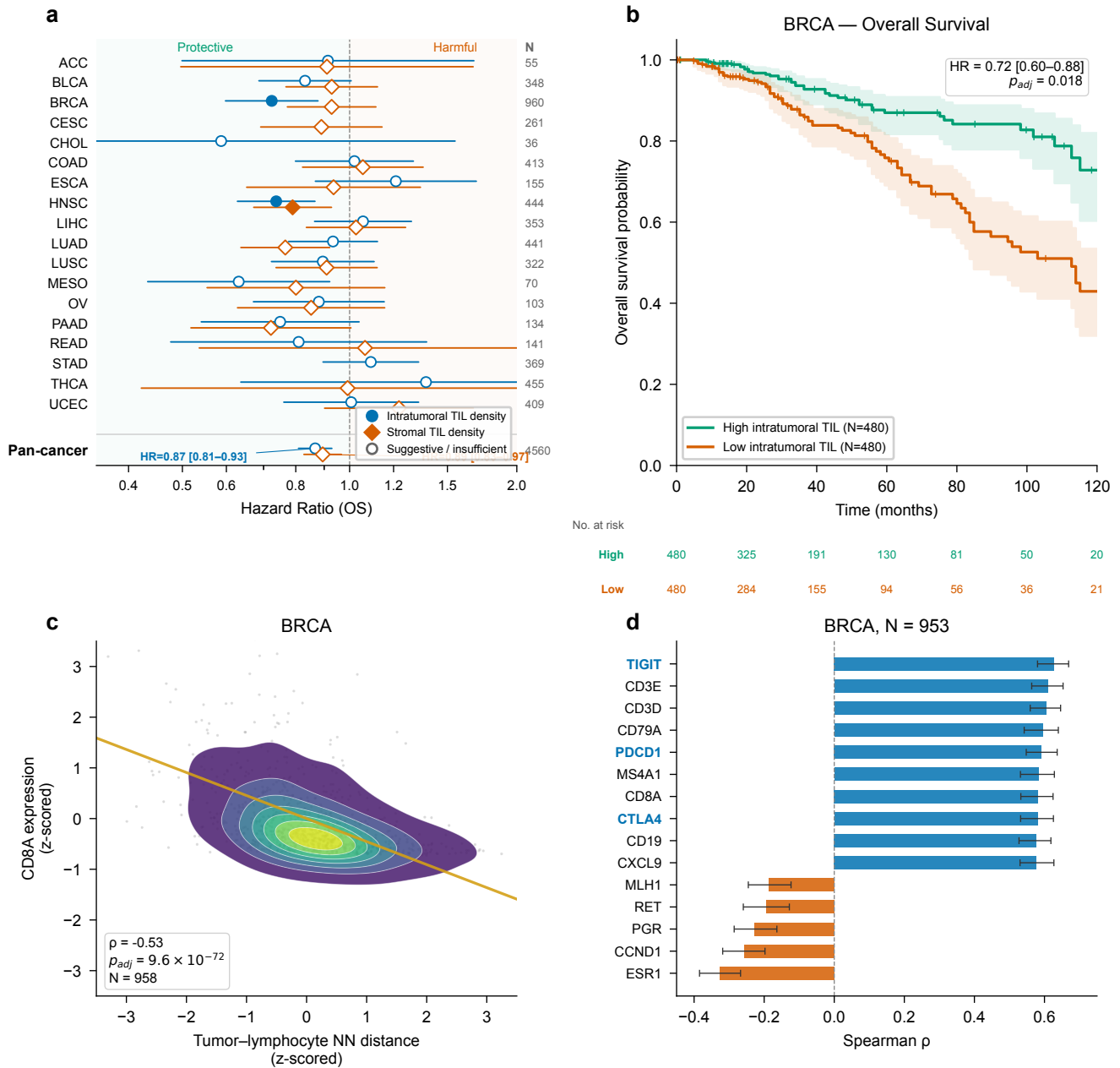


Figure 2: Spatial immune topology reveals compartment-specific prognostic effects. (a) Forest plot of hazard ratios (overall survival, covariate-adjusted Cox regression [age, sex, stage; stratified by TSS]) for intratumoral lymphocyte density (blue circles) and stromal lymphocyte density (orange diamonds) across cancer types and the pan-cancer cohort ($N = 4,560$). Filled markers indicate moderate or strong evidence (BH-adjusted $P < 0.05$ with adequate power); hollow markers indicate suggestive or insufficient evidence. Intratumoral lymphocyte density is protective (HR = 0.87 [0.81, 0.93], $P_{adj} = 9.8 \times 10^{-4}$); stromal lymphocyte density shows a weaker protective effect (HR = 0.89 [0.83, 0.97], $P_{adj} = 0.031$). Error bars represent 95% confidence intervals. Vertical dashed line indicates HR = 1.0 (null). (b) Kaplan–Meier curves for intratumoral lymphocyte density in BRCA (median split, $N = 960$; High: 480, Low: 480), showing a protective association (HR = 0.72 [0.60, 0.88], $P_{adj} = 0.018$). Shaded areas indicate 95% confidence intervals. Number at risk shown below. (c) Tumor–lymphocyte nearest-neighbor distance at the invasive front inversely correlates with CD8A expression in BRCA (Spearman $\rho = -0.53$, $P_{adj} = 1.8 \times 10^{-68}$, $N = 958$), demonstrating that spatial immune exclusion detected by histomics corresponds to reduced cytotoxic T-cell gene expression. Per-slide feature values averaged per case; both axes z-scored within BRCA. (d) Top gene correlates of intratumoral lymphocyte density in BRCA ($N = 953$, adjusted model). Horizontal bar chart showing the top 10 positive and top 5 negative Spearman correlations among significantly associated genes (BH-adjusted $P < 0.05$). Immune checkpoint genes (TIGIT, PDCD1, CTLA4) and T-cell markers (CD3E, CD3D, CD8A, CD8B) dominate the positive correlates, validating the biological identity of the histomic feature. Error bars represent 95% bootstrap confidence intervals. All P -values were calculated using Cox proportional hazards regression (a, b) or Spearman correlation with analytical t -test (c, d), with Benjamini–Hochberg correction for multiple testing within each cancer type.

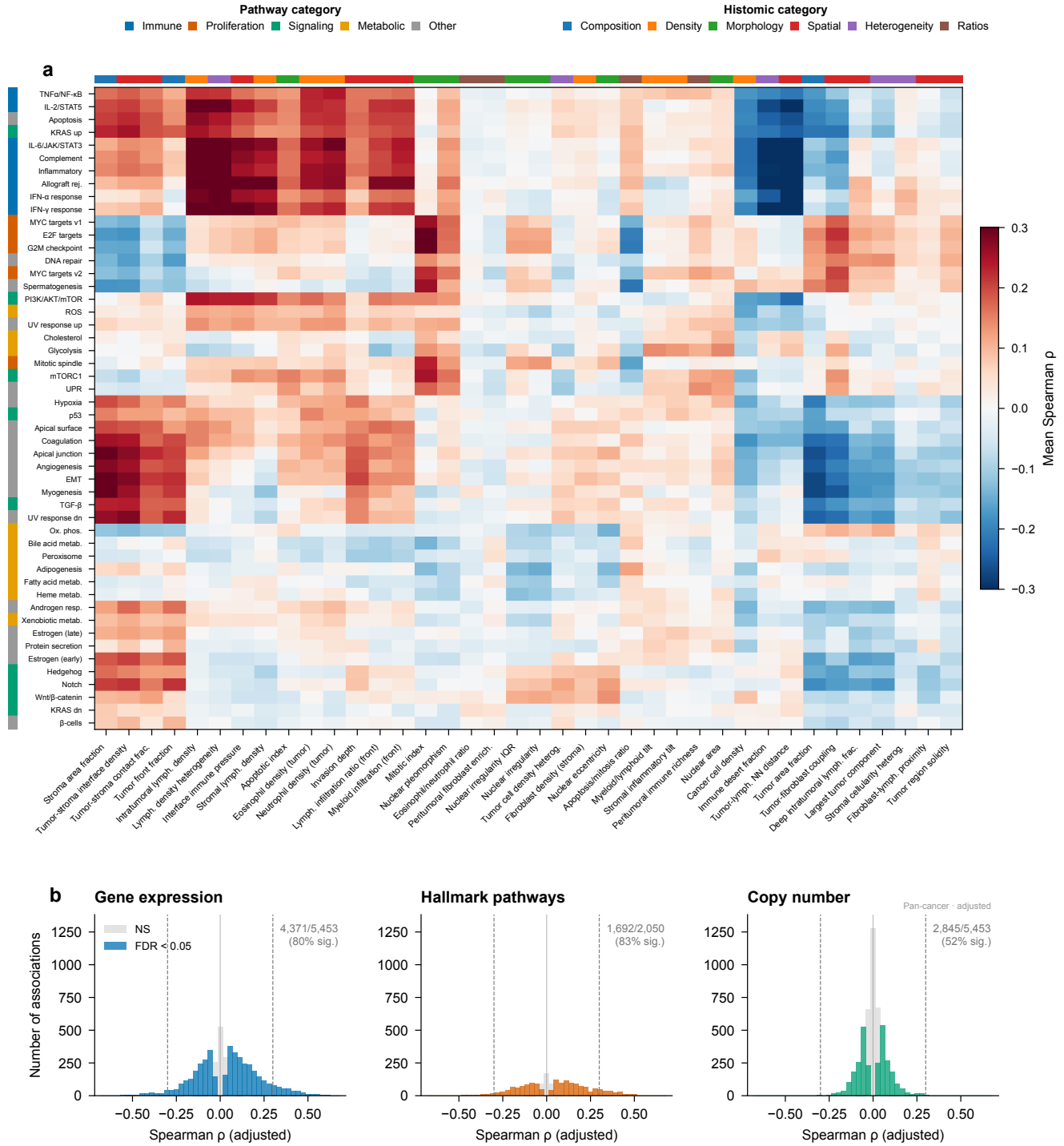


Figure 3: Morphological features recapitulate molecular programs. (a) Heatmap of mean Spearman correlation (across 21 cancer types) between 38 histomic features and 50 Hallmark pathway scores (unadjusted model). Rows and columns are hierarchically clustered (Ward linkage). Left color bar indicates pathway category (Immune, Proliferation, Signaling, Metabolic, Other); top color bar indicates histomic feature category (Composition, Density, Morphology, Spatial, Heterogeneity, Ratios). Structured correspondence is evident: immune cell density features cluster with immune pathway signatures; nuclear morphology and mitotic features cluster with cell cycle and proliferation pathways; invasion depth aligns with EMT. Colormap: RdBu_r, clipped at $\rho = \pm 0.3$. (b) Effect-size distributions for pan-cancer adjusted-model associations, stratified by molecular data type. Each histogram shows the distribution of Spearman ρ values; colored bars indicate significance at FDR < 0.05, gray bars indicate non-significant associations. Vertical dashed lines at $\rho = \pm 0.3$. Gene expression: 4,371/5,453 significant (80%); Hallmark pathways: 1,692/2,050 (83%); copy-number variation: 2,845/5,453 (52%). The higher significance rate among pathway and expression associations, and the broader ρ distributions, reflect stronger morphology–transcriptomic coupling than morphology–genomic coupling. All correlations are Spearman with analytical P -values (t -distribution approximation) and Benjamini–Hochberg correction.

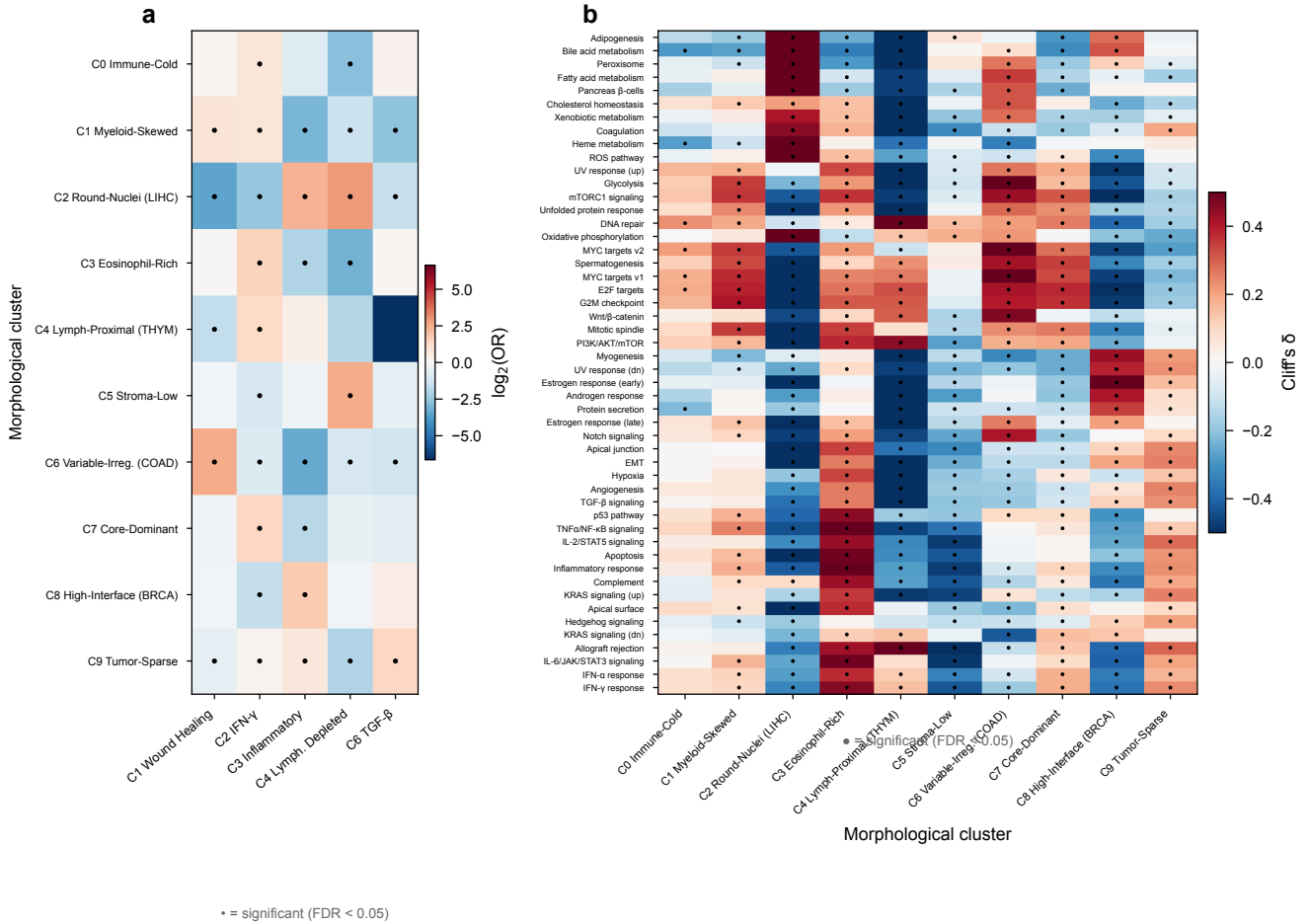


Figure 4: Morphological clusters map to distinct molecular archetypes. (a) Immune subtype enrichment per morphological cluster (L1, pan-cancer). Heatmap of $\log_2(\text{OR})$ from Fisher's exact tests comparing the proportion of each Thorsson immune subtype within each cluster to the remaining cohort. Rows: 10 morphological clusters (labeled with cluster name and dominant cancer type). Columns: five Thorsson immune subtypes (C1 Wound Healing, C2 IFN- γ Dominant, C3 Inflammatory, C4 Lymphocyte Depleted, C6 TGF- β Dominant). Color scale: red–blue diverging, centered at 0. Black dots indicate BH-adjusted $P < 0.05$. Cluster 6 (CRC-enriched) is dominated by C1 Wound Healing ($\text{OR} = 5.59$, $P_{\text{adj}} < 10^{-88}$); Cluster 2 shows combined C4 Lymphocyte Depleted ($\text{OR} = 7.14$) and C3 Inflammatory ($\text{OR} = 4.99$) enrichment (85% combined); Cluster 8 (hormone-driven) is enriched for C3 Inflammatory. (b) Hallmark pathway enrichment (Cliff's δ from Mann–Whitney U tests) per morphological cluster. Rows: 50 Hallmark pathways, hierarchically clustered (Ward linkage). Columns: 10 morphological clusters. Black dots indicate BH-adjusted $P < 0.05$. Cluster 4 (THYM-enriched) shows strong immune rejection pathway enrichment; Cluster 8 shows estrogen response enrichment ($\delta = 0.52$) with suppressed proliferation ($\delta = -0.51$); Cluster 6 shows Wnt/ β -catenin enrichment ($\delta = 0.46$) consistent with CRC composition. Colormap centered at 0, range $[-0.5, 0.5]$.

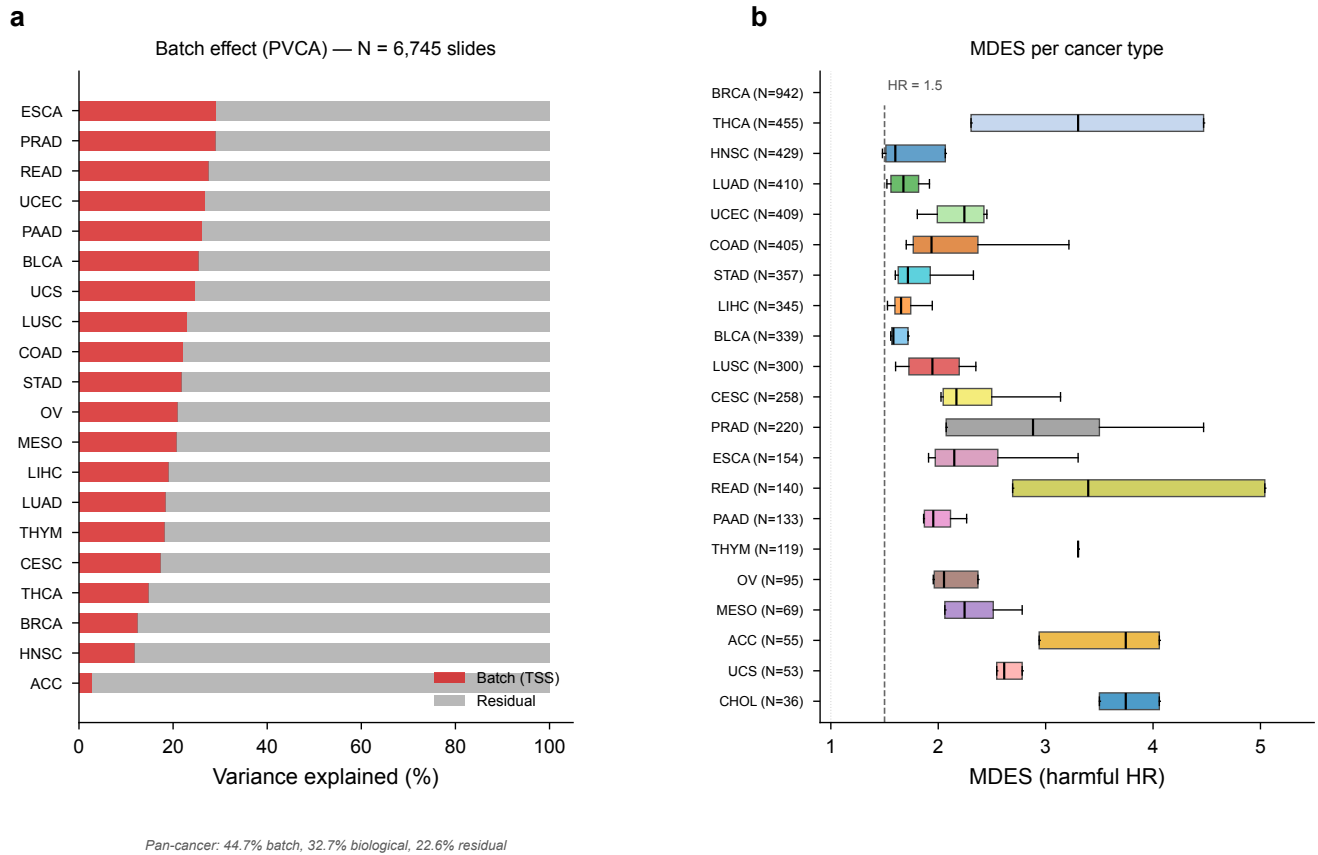


Figure 5: Statistical framework and quality control. (a) PVCA variance decomposition per cancer type showing proportions of variance attributable to batch effects (tissue source site, red) and residual signal (gray). Pan-cancer analysis attributes 44.7% of variance to batch (TSS), 32.7% to biological signal (cancer type), and 22.6% to residual. Within individual cancer types, batch effects account for a median of 20.6% of variance. All per-cancer silhouette scores by TSS are negative (range -0.18 to -0.0004), confirming minimal batch-driven clustering. (b) Minimum detectable effect size (MDES) for harmful hazard ratios across 21 cancer types, ordered by sample size (ascending from bottom). Box plots show the distribution of MDES across features within each cancer type. Well-powered cancer types (BRCA, $N = 960$) can detect $HR \geq 1.62$; underpowered types (CHOL, $N = 36$) require $HR \geq 3.75$ for 80% power. Dashed line indicates the clinically meaningful threshold ($HR = 1.5$). N values per panel: (a) 6,745 slides, 21 cancer types; (b) 5,623 survival associations across 22 cohorts.

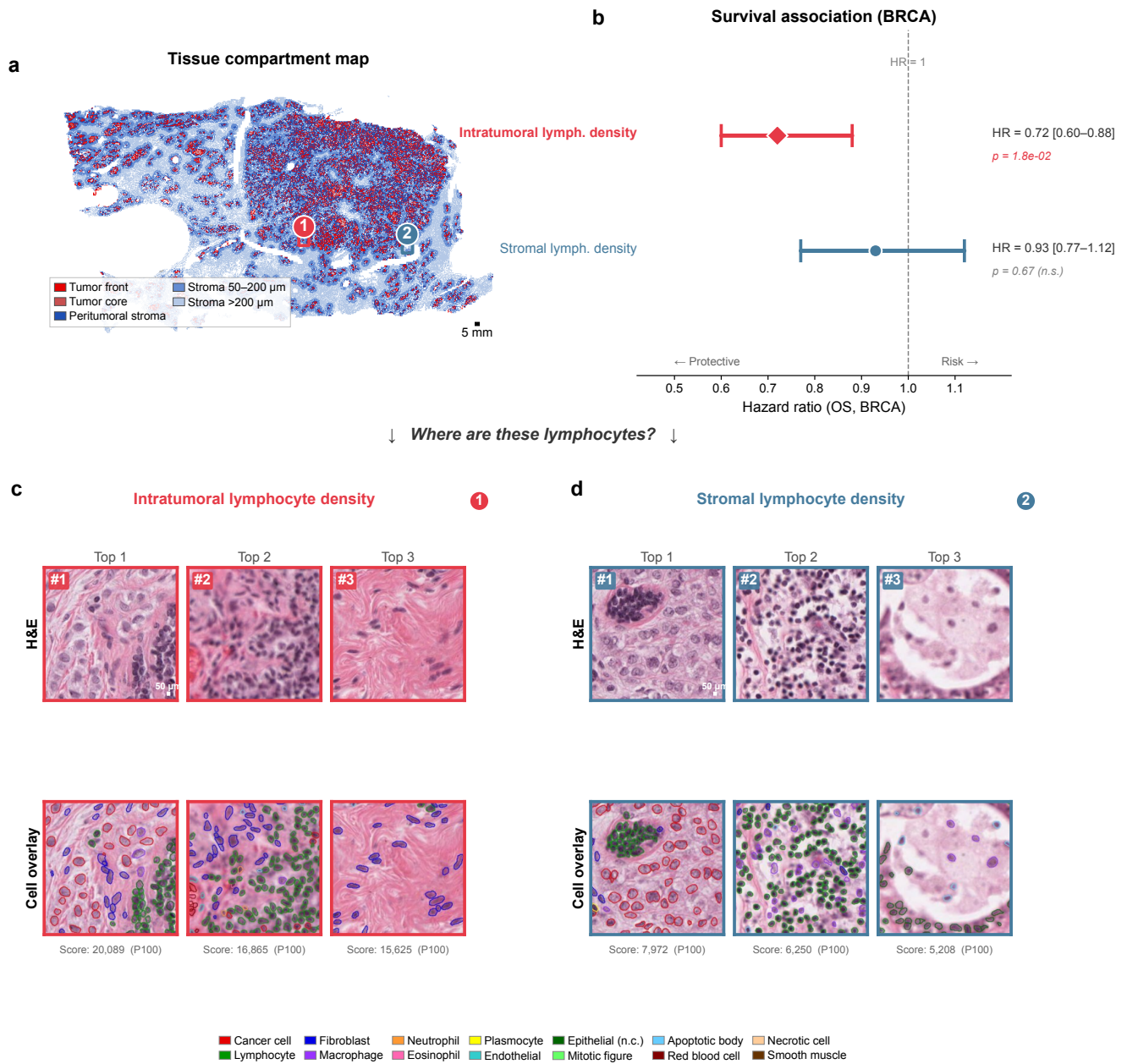


Figure 6: From statistics to cells: spatial interpretability in HistoAtlas. (a) Tissue compartment map for a representative BRCA slide (TCGA-A1-A0SE), showing a nine-class segmentation overlay: tumor front (red), tumor core (dark red), peritumoral stroma at three distance bands (0–50 μm , 50–200 μm , >200 μm ; blue shades), necrosis ring (brown), necrosis (gray), normal epithelium (green), and background (white). Numbered circles mark the tile regions shown in panels (c) and (d). Scale bar: 5 mm. (b) Survival association (covariate-adjusted Cox regression, overall survival) for intratumoral and stromal lymphocyte density in BRCA ($N = 960$). Intratumoral lymphocyte density is protective (HR = 0.72, 95% CI [0.60, 0.88], $P_{\text{adj}} = 0.018$); stromal lymphocyte density is not significant (HR = 0.93, 95% CI [0.77, 1.12], $P_{\text{adj}} = 0.67$). (c) Top-3 ranked tissue tiles for intratumoral lymphocyte density from the same slide, shown as H&E (top) and cell-type prediction overlay (bottom) pairs. Dense green (lymphocyte) annotations among red (cancer cell) annotations confirm high intratumoral immune infiltration. Scale bar: 50 μm . (d) Top-3 ranked tiles for stromal lymphocyte density. Sparser lymphocyte annotations in stromal tissue visually mirror the weaker statistical association. Cell-type overlay legend (14 cell types) is shared between panels (c) and (d).

Supplementary Table 1: Definition of the 40 histomic features extracted per slide (38 used in downstream analyses). Features are organized into five categories: (A) tissue composition, (B) cell densities, (C) nuclear morphology and kinetics, (D) spatial organization, and (E) spatial heterogeneity. Ω_T : tumor compartment; Ω_S : stromal compartment; B_T^{0-50}/B_S^{0-50} : tumor/stromal band within 50 μm of the tumor-stroma boundary; B_S^{50-200} : stromal band 50–200 μm from boundary; d_T : signed distance to tumor boundary (μm); $L(\partial)$: boundary contact length (mm); $\rho_k(R) = n_k(R)/A(R)$: density of cell type k in region R . Features 3 and 24 carry zero signal (zero variance across all slides) and are excluded from all downstream analyses, reducing the working feature set to 38.

No.	Feature	Formula / definition	Unit
<i>(A) Tissue composition</i>			
1	Tumor area fraction	$A(\Omega_T)/A(\Omega)$	fraction
2	Stroma area fraction	$A(\Omega_S)/A(\Omega)$	fraction
3	Normal epithelium area fraction [†]	$A(\Omega_{\text{Norm}})/A(\Omega)$	fraction
4	Eosinophil-neutrophil ratio (peritumoral)	$[n_{\text{Eos}}(B_S^{0-50}) + \epsilon]/[n_{\text{Neu}}(B_S^{0-50}) + \epsilon]$	ratio
<i>(B) Cell densities</i>			
5	Intratumoral cancer cell density	$\rho_{\text{TC}}(\Omega_T)$	cells mm^{-2}
6	Intratumoral lymphocyte density	$\rho_{\text{Ly}}(\Omega_T)$	cells mm^{-2}
7	Stromal lymphocyte density	$\rho_{\text{Ly}}(\Omega_S)$	cells mm^{-2}
8	Intratumoral neutrophil density	$\rho_{\text{Neu}}(\Omega_T)$	cells mm^{-2}
9	Intratumoral eosinophil density	$\rho_{\text{Eos}}(\Omega_T)$	cells mm^{-2}
10	Stromal fibroblast density	$\rho_{\text{Fib}}(\Omega_S)$	cells mm^{-2}
<i>(C) Nuclear morphology and kinetics</i>			
11	Tumor nuclear area (median)	median(A_i) over tumor nuclei	μm^2
12	Tumor pleomorphism index	$\text{IQR}(A_i)/[\text{median}(A_i) + \epsilon]$	unitless
13	Tumor nuclear eccentricity (median)	median(e_i) over tumor nuclei	unitless
14	Tumor nuclear irregularity (median)	median($P_i^2/4\pi A_i$)	unitless
15	Tumor nuclear irregularity (IQR)	$\text{IQR}(P_i^2/4\pi A_i)$	unitless
16	Mitotic index (tumor)	$n_{\text{Mit}}(\Omega_T)/n_{\text{TC}}(\Omega_T) \times 10^3$	per 1 k TC
17	Apoptotic index (tumor)	$n_{\text{Apop}}(\Omega_T)/n_{\text{TC}}(\Omega_T) \times 10^3$	per 1 k TC
18	Apoptosis-mitosis ratio	$[n_{\text{Apop}} + \epsilon]/[n_{\text{Mit}} + \epsilon]$ in Ω_T	ratio
<i>(D) Spatial organization</i>			
19	Largest tumor component share	$\max_j A(C_j)/A(\Omega_T)$	fraction
20	Tumor region solidity	$A(C_{\text{max}})/A(\text{Hull}(C_{\text{max}}))$	unitless
21	Tumor-stroma interface density	$L(\partial(T, S))/A(\Omega_T)$	mm^{-1}
22	Tumor front fraction	$A(B_T^{0-50})/A(\Omega_T)$	fraction
23	Tumor-stroma contact fraction	$L(\partial(T, S))/\sum_{c \neq T} L(\partial(T, c))$	fraction
24	Tumor-normal contact fraction [†]	$L(\partial(T, N))/\sum_{c \neq T} L(\partial(T, c))$	fraction
25	Lymphocyte infiltration ratio (front)	$\rho_{\text{Ly}}(B_T^{0-50})/[\rho_{\text{Ly}}(B_S^{0-50}) + \epsilon]$	ratio
26	Myeloid infiltration ratio (front)	$\rho_{\text{Mye}}(B_T^{0-50})/[\rho_{\text{Mye}}(B_S^{0-50}) + \epsilon]$	ratio
27	Deep intratumoral lymphocyte fraction	$n_{\text{Ly}}(d_T > 50)/n_{\text{Ly}}(\Omega_T)$	fraction
28	Peritumoral immune richness	No. immune types with ≥ 5 cells in B_S^{0-50}	count (0–4)
29	Immune desert fraction	$A(\{x \in \Omega_T : d_{\text{Ly}} > 200 \mu\text{m}\})/A(\Omega_T)$	fraction
30	Intratumoral myeloid-lymphoid tilt	$[n_{\text{Neu}} + n_{\text{Eos}}]/[n_{\text{Ly}} + n_{\text{Pla}} + \epsilon]$ in Ω_T	ratio
31	Interface-normalized immune pressure	$n_{\text{Ly}}(B_S^{0-50} \cup B_T^{0-50})/L(\partial(T, S))$	cells mm^{-1}
32	Invasion depth (75th pctl)	p75 of $-d_T(\rho_i)$ for TC in stroma	μm
33	Tumor-fibroblast coupling (front)	Median NN dist., TC to Fib in B_T^{0-50}	μm
34	Tumor-lymphocyte NN distance (front)	Median NN dist., TC to Ly in B_T^{0-50}	μm
35	Peritumoral fibroblast enrichment	$\rho_{\text{Fib}}(B_S^{0-50})/[\rho_{\text{Fib}}(B_S^{50-200}) + \epsilon]$	ratio
36	Stromal inflammatory tilt	$[n_{\text{Neu}} + n_{\text{Eos}}]/[n_{\text{Ly}} + n_{\text{Pla}} + \epsilon]$ in Ω_S	ratio
37	Fibroblast-lymphocyte proximity (stroma)	Median NN dist., Ly to Fib in Ω_S	μm
<i>(E) Spatial heterogeneity</i>			
38	Tumor cell density heterogeneity	CV of ρ_{TC} across tumor tiles	CV
39	Lymphocyte density heterogeneity (tumor)	CV of ρ_{Ly} across tumor tiles	CV
40	Stromal cellularity heterogeneity	CV of total cell density across stromal tiles	CV

[†] Zero signal across all slides; excluded from downstream analyses (see Methods). Abbreviations: TC, tumor cells; Ly, lymphocytes; Neu, neutrophils; Eos, eosinophils; Fib, fibroblasts; Pla, plasmocytes; Mit, mitotic figures; Apop, apoptotic bodies; Mye, myeloid cells (Neu + Eos); NN, nearest-neighbor; CV, coefficient of variation; Hull, convex hull; $\epsilon = 10^{-6}$.

Supplementary Table 2: Biological plausibility audit of 60 atlas-derived claims. Each atomic claim was assessed against the published literature and assigned an evidence level: WE = well-established (>3 independent confirmations); SUP = supported (1–3 prior studies consistent); NP = novel, biologically plausible (no prior report, mechanistically coherent); NU = novel, uncertain (no prior report, mechanism unclear); C = contradicted (apparent contradiction, resolved by category distinction). Overall: 27 WE (45%), 15 SUP (25%), 12 NP (20%), 5 NU (8%), 1 C (2%).

ID	Axis	Claim	Evid.	Key statistic	Cancer	References
1.1	Immune	Higher intratumoral TIL density → better OS in BRCA	WE	HR = 0.72 (0.60–0.88), adj.	BRCA	(13, 50, 51)
1.2	Immune	Higher intratumoral TIL density → better OS pan-cancer	WE	HR = 0.87 (0.81–0.93), adj.	PAN	(11, 13)
1.3	Immune	Stromal lymphocyte density shows weaker protective effect than intratumoral pan-cancer	SUP	HR = 0.89 (0.83–0.97), adj.	PAN	(51)
1.4	Immune	Compartment-specific prognostic strength: intratumoral > stromal	NP	IT HR = 0.87 vs S HR = 0.89, adj.	PAN	(13)
1.5	Immune	Immune desert fraction predicts worse OS in LIHC	SUP	HR = 1.29 (1.12–1.48)	LIHC	(56)
1.6	Immune	Deep intratumoral lymphocyte fraction protective in HNSC	SUP	HR = 0.79 (0.68–0.91)	HNSC	(11)
1.7	Immune	Interface-normalized immune pressure protective in HNSC (adjusted)	NP	HNSC HR = 0.74	HNSC	(11)
1.8	Immune	Peritumoral immune richness has no prognostic value	NU	NS all cancers	PAN	(11)
1.9	Immune	Top gene correlates are T-cell markers and checkpoints	WE	$\rho = 0.58–0.63$	BRCA	(10)
1.10	Immune	Stromal TILs correlate with effector/IFN- γ genes	SUP	$\rho = 0.49–0.53$	BRCA	(89)
1.11	Immune	B-cell markers among top TIL correlates	SUP	$\rho(\text{CD79A}) = 0.60$	BRCA	(89, 90)
1.12	Immune	Immune subtypes associate with morphometric TIL density	WE	$\eta^2 = 0.12–0.13$	BRCA	(10)
2.1	Prolif.	High mitotic index → worse OS pan-cancer	WE	HR = 1.25 (1.19–1.31)	PAN	(43)
2.2	Prolif.	CCNE1 is top correlate of mitotic index in BRCA	WE	$\rho = 0.57$	BRCA	
2.3	Prolif.	PLK1, AURKA, BIRC5 are canonical mitotic correlates	WE	$\rho = 0.52–0.65$	Multi	(52)
2.4	Prolif.	MKI67 and TOP2A validate morphometric mitotic index	WE	$\rho = 0.48–0.60$	Multi	
2.5	Prolif.	Apoptotic index protective in LIHC	SUP	HR = 0.66 (0.55–0.79)	LIHC	
2.6	Prolif.	Apoptosis/mitosis ratio protective pan-cancer	SUP	HR = 0.79 (0.75–0.84)	PAN	
2.7	Prolif.	ACC has extreme cell turnover sensitivity	NP	Ratio HR = 0.36 (0.20–0.66)	ACC	
2.8	Prolif.	APC negatively correlates with mitotic index in STAD	WE	$\rho = -0.24$	STAD	
2.9	Prolif.	Tumor cell density heterogeneity null pan-cancer	NU	HR \approx 1.00, NS	PAN	(55)
2.10	Prolif.	Reversed mitotic index effects in COAD, ESCA, OV	NU	HR \approx 0.78, NS	Multi	
3.1	Nuclear	Larger nuclei → worse OS pan-cancer	WE	HR = 1.19, $P = 5 \times 10^{-12}$	PAN	(29, 43)
3.2	Nuclear	Nuclear area predicts OS in HCC	WE	HR = 1.20	LIHC	
3.3	Nuclear	Pleomorphism correlates with PLK1, AURKA, CCNE1, MKI67	WE	$\rho = 0.40–0.49$	BRCA	(52)
3.4	Nuclear	Pleomorphism inversely correlates with BCL2 and ESR1	WE	$\rho = -0.36$ to -0.37	BRCA	
3.5	Nuclear	Nuclear eccentricity has opposing tissue-specific effects	NP	UCEC HR = 0.70; LIHC HR = 1.32	Multi	(29)
3.6	Nuclear	Nuclear irregularity IQR predicts OS only in LIHC	NP	HR = 1.41	LIHC	
3.7	Nuclear	Nuclear irregularity protective in HNSC	NU	HR = 0.78	HNSC	
4.1	Invasion	Greater invasion depth → worse OS pan-cancer	WE	HR = 1.11	PAN	
4.2	Invasion	Invasion depth correlates with EMT markers	WE	$\rho(\text{ZEB1}) = 0.32$	BRCA	(42)
4.3	Invasion	Invasion depth correlates with ALDH1A1	SUP	$\rho = 0.21$	BRCA	
4.4	Invasion	TGFB1 correlates with invasion in BRCA and PAAD	WE	$\rho = 0.29$	Multi	(42)
4.5	Invasion	Invasion depth inversely correlates with proliferation	SUP	$\rho(\text{E2F targets}) = -0.30$	BRCA	(44, 45)
4.6	Invasion	Tumor–stroma interface density protective pan-cancer	NP	HR = 0.85, $P = 1 \times 10^{-8}$	PAN	
4.7	Invasion	Fibroblast coupling at front predicts OS in LIHC	SUP	HR = 1.48, $P = 7 \times 10^{-5}$	LIHC	(54)
5.1	Stromal	Eosinophil infiltration protective in BRCA and HNSC	WE	BRCA HR = 0.63; HNSC HR = 0.77	Multi	(53)
5.2	Stromal	Eosinophil density correlates with cytotoxic T-cell signatures	WE	$\rho(\text{GZMB}) = 0.40$	BRCA	(53)
5.3	Stromal	Neutrophil density is context-dependent	WE	NS pan-cancer	PAN	
5.4	Stromal	Eosinophil/neutrophil ratio captures innate immune polarization	NP	BRCA HR = 0.65	BRCA	
5.5	Stromal	Fibroblast density non-prognostic pan-cancer	SUP	HR = 0.97	PAN	(54)
5.6	Stromal	Stromal inflammatory tilt non-prognostic	NU	NS all cancers	PAN	
6.1	Spatial	Lymphocyte density at invasive front predicts improved OS	WE	HR = 0.85, $P = 1 \times 10^{-8}$	PAN	(11, 12)
6.2	Spatial	NN distance captures spatial immune exclusion	SUP	$\rho(\text{cytotoxic}) = -0.54$	BRCA	(91)
6.3	Spatial	Greater NN distance → worse gene expression signatures	WE	$\rho(\text{CD8A}) = -0.53$	BRCA	(41, 91)
6.4	Spatial	Myeloid-to-lymphoid tilt adversely prognostic	SUP	HR = 1.10, $P = 3 \times 10^{-5}$	PAN	(10)
6.5	Spatial	Lymphocyte infiltration at front correlates with B-cell signatures	SUP	$\rho(\text{B-cell}) = 0.49$	BRCA	(89, 90)
6.6	Spatial	Myeloid infiltration at front independently protective	NP	HR = 0.92	PAN	
6.7	Spatial	NN distance at front associated with worse OS in LUAD (unadjusted only)	NP	HR = 1.29 (unadj); NS adjusted	LUAD	
7.1	Tissue	Tumor area fraction is a proxy for tumor purity	WE	$\rho(\text{prolif}) = 0.40$	PAN	(92)
7.2	Tissue	Normal epithelium near-zero in resected tumors	WE	–	PAN	
7.3	Tissue	Lymphocyte density heterogeneity (spatial CV) is protective	NP	HR = 0.74 (LIHC); HR = 0.82 (HNSC)	Multi	(57)
7.4	Tissue	Stromal cellularity heterogeneity protective in UCEC	NP	HR = 0.61	UCEC	

Continued on next page

Supplementary Table 2 continued

ID	Axis	Claim	Evid.	Key statistic	Cancer	References
7.5	Tissue	Morphological heterogeneity is protective (contradicts ITH paradigm)	C	Protective in 11/15 cancers (adjusted)	PAN	(55)
7.6	Tissue	Tumor area fraction non-prognostic pan-cancer	WE	HR = 1.01, NS	PAN	(92)
8.1	Cluster	Immune-hot clusters enriched for C2 (IFN- γ)	WE	Clusters 3, 4, 7 all C2+	PAN	(10)
8.2	Cluster	Proliferative clusters have worse survival	WE	$r \approx 0.85$ across clusters	PAN	(43)
8.3	Cluster	Tissue-specific clusters recapitulate organ pathways	WE	THYM \rightarrow immune rejection; CRC \rightarrow Wnt/ β -catenin	PAN	(36, 37)
8.4	Cluster	Mutation enrichment reflects TMB, not specific drivers	SUP	Binary enrich/deplete pattern	PAN	
8.5	Cluster	Two distinct immune-cold phenotypes with opposite survival	NP	C2: HR = 0.54; C8: HR = 1.37	PAN	

Supplementary Table 3: TCGA cancer types included and excluded from the HistoAtlas analysis. Twenty-one solid-tumor cancer types were included. Twelve additional cancer types were excluded because their dominant cell morphologies fall outside the training domain of the cell detection model.

Abbreviation	Full name	<i>N</i> slides	Status
ACC	Adrenocortical carcinoma	227	Included
BLCA	Bladder urothelial carcinoma	417	Included
BRCA	Breast invasive carcinoma	1,037	Included
CESC	Cervical squamous cell carcinoma	279	Included
CHOL	Cholangiocarcinoma	38	Included
COAD	Colon adenocarcinoma	441	Included
ESCA	Esophageal carcinoma	158	Included
HNSC	Head and neck squamous cell carcinoma	471	Included
LIHC	Liver hepatocellular carcinoma	365	Included
LUAD	Lung adenocarcinoma	511	Included
LUSC	Lung squamous cell carcinoma	357	Included
MESO	Mesothelioma	82	Included
OV	Ovarian serous cystadenocarcinoma	107	Included
PAAD	Pancreatic adenocarcinoma	146	Included
PRAD	Prostate adenocarcinoma	353	Included
READ	Rectum adenocarcinoma	157	Included
STAD	Stomach adenocarcinoma	400	Included
THCA	Thyroid carcinoma	473	Included
THYM	Thymoma	180	Included
UCEC	Uterine corpus endometrial carcinoma	459	Included
UCS	Uterine carcinosarcoma	87	Included
DLBC	Diffuse large B-cell lymphoma	–	Excluded (lymphoid cells)
GBM	Glioblastoma multiforme	–	Excluded (glial cells)
KICH	Kidney chromophobe	–	Excluded (renal tubular)
KIRC	Kidney renal clear cell carcinoma	–	Excluded (renal tubular)
KIRP	Kidney renal papillary cell carcinoma	–	Excluded (renal tubular)
LAML	Acute myeloid leukemia	–	Excluded (myeloid blasts)
LGG	Brain lower grade glioma	–	Excluded (glial cells)
PCPG	Pheochromocytoma and paraganglioma	–	Excluded (neuroendocrine)
SARC	Sarcoma	–	Excluded (mesenchymal)
SKCM	Skin cutaneous melanoma	–	Excluded (melanocytes)
TGCT	Testicular germ cell tumors	–	Excluded (germ cells)
UVM	Uveal melanoma	–	Excluded (melanocytes)

Supplementary Table 4: Curated gene panel (133 genes) used for molecular correlation analysis. Genes were selected from established cancer gene panels, immune checkpoint targets, and EMT/stemness markers. Functional categories are provided for annotation; genes may participate in multiple pathways.

Category	Genes
Immune / checkpoint (36)	CD274 (PD-L1), PDCD1 (PD-1), PDCD1LG2 (PD-L2), CTLA4, LAG3, TIGIT, HAVCR2 (TIM-3), IDO1, CD8A, CD8B, CD4, CD3D, CD3E, FOXP3, CD19, CD79A, MS4A1 (CD20), CD14, CD68, CD163, CD40, CD80, CD86, ITGAM, NKG7, IFNG, GZMA, GZMB, PRF1, TNF, IL6, IL10, IL2, CXCL9, CXCL10, TGFB1
Proliferation / cell cycle (15)	MKI67, TOP2A, PCNA, CCNB1, CCND1, CCNE1, CDK1, CDK2, CDK4, CDK6, PLK1, AURKA, BIRC5, MCM2, E2F1
EMT / invasion / stemness (15)	CDH1, CDH2, VIM, SNAI1, SNAI2, ZEB1, ZEB2, TWIST1, FN1, ACTA2, ALDH1A1, CD44, SOX2, NANOG, PROM1
Apoptosis / DNA damage (19)	TP53, BCL2, BCL2L1, MCL1, BAX, CASP3, CASP8, FAS, BRCA1, BRCA2, ATM, CHEK1, CHEK2, RAD51, PARP1, MLH1, MSH2, MSH6, CDKN2A
Signaling / oncogenes (27)	EGFR, ERBB2 (HER2), MET, KRAS, NRAS, HRAS, BRAF, NF1, PIK3CA, PTEN, AKT1, MTOR, NOTCH1, FBXW7, CTNNB1, APC, SMAD4, RB1, MYC, ALK, RET, FGFR1, FGFR2, FGFR3, KIT, PDGFRA, JAK2
Hormone receptors (3)	ESR1, PGR, AR
Epigenetic / chromatin (6)	ARID1A, SMARCA4, IDH1, IDH2, SETD2, BAP1
Metabolism / hypoxia (5)	VEGFA, HIF1A, LDHA, SLC2A1, CA9
Other (7)	NFE2L2, KEAP1, STK11, NF2, VHL, MGMT, TERT

Gene names follow HUGO Gene Nomenclature Committee (HGNC) conventions. Common aliases are shown in parentheses.

Supplementary Table 5: 50 MSigDB Hallmark pathways used for ssGSEA scoring. Pathway activity scores were computed via single-sample Gene Set Enrichment Analysis (ssGSEA) (76, 93) using the 50 Hallmark gene sets from MSigDB (34) (collection identifier: h. a11, available at https://www.gsea-msigdb.org/gsea/msigdb/collection_details.jsp). Each Hallmark gene set contains ~200 genes (range: 32–200) and represents a well-characterized biological process or state. Gene sets with fewer than 10 genes present in the expression matrix after intersection were excluded. Full gene lists for all 50 Hallmark pathways are available from MSigDB (Liberzon et al., 2015).

MSigDB Hallmark pathway	Biological category
HALLMARK_ADIPOGENESIS	Metabolic
HALLMARK_ALLOGRAFT_REJECTION	Immune
HALLMARK_ANDROGEN_RESPONSE	Hormonal
HALLMARK_ANGIOGENESIS	Development
HALLMARK_APICAL_JUNCTION	Cellular component
HALLMARK_APICAL_SURFACE	Cellular component
HALLMARK_APOPTOSIS	Proliferation
HALLMARK_BILE_ACID_METABOLISM	Metabolic
HALLMARK_CHOLESTEROL_HOMEOSTASIS	Metabolic
HALLMARK_COAGULATION	Immune
HALLMARK_COMPLEMENT	Immune
HALLMARK_DNA_REPAIR	DNA damage
HALLMARK_E2F_TARGETS	Proliferation
HALLMARK_EPITHELIAL_MESENCHYMAL_TRANSITION	Development
HALLMARK_ESTROGEN_RESPONSE_EARLY	Hormonal
HALLMARK_ESTROGEN_RESPONSE_LATE	Hormonal
HALLMARK_FATTY_ACID_METABOLISM	Metabolic
HALLMARK_G2M_CHECKPOINT	Proliferation
HALLMARK_GLYCOLYSIS	Metabolic
HALLMARK_HEDGEHOG_SIGNALING	Signaling
HALLMARK_HEME_METABOLISM	Metabolic
HALLMARK_HYPOXIA	Metabolic
HALLMARK_IL2_STAT5_SIGNALING	Immune
HALLMARK_IL6_JAK_STAT3_SIGNALING	Immune
HALLMARK_INFLAMMATORY_RESPONSE	Immune
HALLMARK_INTERFERON_ALPHA_RESPONSE	Immune
HALLMARK_INTERFERON_GAMMA_RESPONSE	Immune
HALLMARK_KRAS_SIGNALING_DN	Signaling
HALLMARK_KRAS_SIGNALING_UP	Signaling
HALLMARK_MITOTIC_SPINDLE	Proliferation
HALLMARK_MTORC1_SIGNALING	Signaling
HALLMARK_MYC_TARGETS_V1	Proliferation
HALLMARK_MYC_TARGETS_V2	Proliferation
HALLMARK_MYOGENESIS	Development
HALLMARK_NOTCH_SIGNALING	Signaling
HALLMARK_OXIDATIVE_PHOSPHORYLATION	Metabolic
HALLMARK_P53_PATHWAY	Proliferation
HALLMARK_PANCREAS_BETA_CELLS	Development
HALLMARK_PEROXISOME	Metabolic
HALLMARK_PI3K_AKT_MTOR_SIGNALING	Signaling
HALLMARK_PROTEIN_SECRETION	Cellular component
HALLMARK_REACTIVE_OXYGEN_SPECIES_PATHWAY	Metabolic
HALLMARK_SPERMATOGENESIS	Development
HALLMARK_TGF_BETA_SIGNALING	Signaling
HALLMARK_TNFA_SIGNALING_VIA_NFKB	Immune
HALLMARK_UNFOLDED_PROTEIN_RESPONSE	Cellular component
HALLMARK_UV_RESPONSE_DN	DNA damage
HALLMARK_UV_RESPONSE_UP	DNA damage
HALLMARK_WNT_BETA_CATENIN_SIGNALING	Signaling
HALLMARK_XENOBIOTIC_METABOLISM	Metabolic

Supplementary Table 6: Benjamini–Hochberg correction family definitions by analysis type. Each family groups biologically coherent tests to control the false discovery rate within meaningful contexts. Every adjusted *P*-value is stored alongside its correction family identifier and the number of tests in the family.

Analysis type	Family definition	Typical family size
Survival (Cox)	Cancer type × endpoint × model	36–38
Survival (RMST)	Cancer type × endpoint × model	36–38
Molecular correlations	Cancer type × target set × method × model	133–293
Categorical associations	Cancer type × variable × test type × model	36–38
Cluster survival (Cox)	Cluster level × analysis type × cancer × endpoint × model	10–69
Cluster survival (log-rank)	Cluster level × analysis type × cancer × endpoint	10–69
Cluster enrichment (mutation)	Cluster level × cancer type	50–133
Cluster enrichment (pathway)	Cluster level × cancer type	50
GSEA	Canonical FDR (pooled null NES)	All gene sets

Supplementary Table 7: Proportional hazards assumption violation prevalence. For each cancer type and survival endpoint, the fraction of fitted Cox models classified as “pass” ($P \geq 0.05$), “warn” ($0.01 \leq P < 0.05$), or “fail” ($P < 0.01$) based on the Schoenfeld residual test. When the PH assumption failed, restricted mean survival time (RMST) was computed as a complementary summary. Values shown for the adjusted model (age, sex, stage; stratified by tissue source site); unadjusted models show similar patterns.

Cancer type	<i>N</i> models	Pass (%)	Warn (%)	Fail (%)
ACC	114	112 (98)	2 (2)	0 (0)
BLCA	152	145 (95)	7 (5)	0 (0)
BRCA	152	141 (93)	9 (6)	2 (1)
CESC	152	135 (89)	8 (5)	9 (6)
CHOL	114	109 (96)	5 (4)	0 (0)
COAD	152	145 (95)	4 (3)	3 (2)
ESCA	152	142 (93)	9 (6)	1 (1)
HNSC	152	144 (95)	6 (4)	2 (1)
LIHC	152	140 (92)	5 (3)	7 (5)
LUAD	152	145 (95)	6 (4)	1 (1)
LUSC	152	135 (89)	12 (8)	5 (3)
MESO	114	112 (98)	2 (2)	0 (0)
OV	152	142 (93)	7 (5)	3 (2)
PAAD	152	151 (99)	1 (1)	0 (0)
PRAD	76	69 (91)	4 (5)	3 (4)
READ	114	113 (99)	1 (1)	0 (0)
STAD	152	136 (89)	13 (9)	3 (2)
THCA	113	110 (97)	3 (3)	0 (0)
THYM	38	35 (92)	2 (5)	1 (3)
UCEC	152	147 (97)	5 (3)	0 (0)
PANCAN	152	107 (70)	16 (11)	29 (19)
Total	2,811	2,615 (93.0)	127 (4.5)	69 (2.5)

N models: number of adjusted Cox regressions (features \times endpoints available for each cancer type). UCS is excluded because the adjusted model did not converge for this cohort. Not all endpoints are evaluable in all cancer types; see Supplementary Table 9 for horizon definitions. Pass: Schoenfeld $P \geq 0.05$; Warn: $0.01 \leq P < 0.05$; Fail: $P < 0.01$. Unadjusted models show similar patterns. The pan-cancer cohort exhibits the highest violation rate because cancer-type heterogeneity introduces non-proportional baseline hazards.

Supplementary Table 8: Sample sizes per cancer type and model tier for overall survival. Sample sizes for the unadjusted (feature only) and adjusted (feature + age + sex + stage; TSS-stratified) models. When MICE imputation was used, sample sizes reflect the imputed dataset; differences between tiers reflect cancer types where the adjusted model was not fitted due to insufficient covariate data.

Cancer type	<i>n</i> (unadjusted)	<i>n</i> (adjusted)	MICE used
ACC	55	55	Yes
BLCA	348	348	Yes
BRCA	960	960	Yes
CESC	261	261	No [‡]
CHOL	36	36	No
COAD	413	413	Yes
ESCA	155	155	Yes
HNSC	444	444	Yes
LIHC	353	353	Yes
LUAD	441	441	Yes
LUSC	322	322	Yes
MESO	70	70	No
OV	103	103	No [‡]
PAAD	134	134	Yes
READ	141	141	Yes
STAD	369	369	Yes
THCA	455	455	Yes
UCEC	409	409	Yes [‡]
UCS	53	–	–
PANCAN	5,957	4,560	No

PRAD and THYM are omitted because OS was not evaluable for these cancer types (see Supplementary Table 9). UCS is marked “–” because the adjusted model did not converge for this cohort. For cancer types where MICE was used, the *n* (adjusted) reflects the imputed dataset (5 imputations, pooled via Rubin’s rules); the *n* (unadjusted) column uses complete cases for the feature and survival outcome only. [‡] CESC, OV, and UCEC use age and sex only as covariates (pathologic stage was unavailable); all other adjusted models include age, sex, and stage. PANCAN uses complete-case analysis (no MICE); the reduced *n* (adjusted) reflects exclusion of cases with missing stage data.

Supplementary Table 9: Cancer-type-specific RMST time horizons. The restricted mean survival time (RMST) was computed using cancer-type-specific truncation horizons chosen to ensure adequate follow-up and at-risk populations.

Cancer type	Horizon (days)	Rationale
PAAD	730 (2 yr)	Aggressive; short median survival
MESO	730 (2 yr)	Aggressive; short median survival
THCA	1825 (5 yr)	Indolent; long median survival
PRAD	1825 (5 yr)	Indolent; long median survival
All others	1095 (3 yr)	Default

Supplementary Table 10: Descriptive statistics for the 38 histomic features across 6,745 slides. Feature numbering follows Supplementary Table 1; features 3 and 24 (zero variance) are excluded. Cell density, nearest-neighbor distance, and heterogeneity features are reported on a \log_e -transformed scale (see Methods, §4.3). IQR: interquartile range (Q1–Q3).

No.	Feature	Min	Max	Mean	Std	Median	IQR
<i>(A) Tissue composition</i>							
1	Tumor area fraction	0.04	0.93	0.45	0.20	0.43	0.29–0.60
2	Stroma area fraction	0.02	0.92	0.45	0.22	0.46	0.28–0.62
4	Eos/neu ratio (peritumoral)	0.00	2.70	0.40	0.47	0.22	0.09–0.52
<i>(B) Cell densities (log scale)</i>							
5	Cancer cell density (IT)	5.15	9.39	8.37	0.58	8.47	8.10–8.75
6	Lymphocyte density (IT)	2.52	10.01	6.03	1.40	6.00	5.08–6.96
7	Lymphocyte density (S)	3.81	7.92	6.11	0.82	6.17	5.56–6.73
8	Neutrophil density (IT)	0.00	6.87	2.39	1.58	2.14	1.09–3.47
9	Eosinophil density (IT)	0.00	5.25	1.41	1.31	0.98	0.30–2.32
10	Fibroblast density (S)	5.69	8.94	7.41	0.53	7.42	7.09–7.74
<i>(C) Nuclear morphology and kinetics</i>							
11	Nuclear area (median)	16.59	72.24	38.72	9.93	37.50	31.75–44.75
12	Pleomorphism index	0.33	1.19	0.67	0.15	0.66	0.58–0.76
13	Nuclear eccentricity	0.52	0.81	0.71	0.05	0.72	0.69–0.75
14	Nuclear irregularity (median)	1.06	1.33	1.16	0.05	1.15	1.13–1.19
15	Nuclear irregularity (IQR)	0.05	0.45	0.18	0.07	0.17	0.14–0.21
16	Mitotic index	0.00	2.42	0.75	0.66	0.61	0.13–1.27
17	Apoptotic index	0.99	6.61	3.35	0.93	3.33	2.76–3.89
18	Apoptosis/mitosis ratio	0.82	8.12	3.59	1.61	3.31	2.33–4.66
<i>(D) Spatial organization</i>							
19	Largest tumor component	0.01	0.99	0.32	0.26	0.24	0.11–0.46
20	Tumor region solidity	0.21	0.84	0.50	0.13	0.49	0.41–0.58
21	T–S interface density	0.46	89.50	25.59	18.19	21.85	11.64–35.66
22	Tumor front fraction	0.04	1.00	0.54	0.26	0.55	0.32–0.76
23	T–S contact fraction	0.01	0.80	0.34	0.18	0.34	0.20–0.47
25	Ly infiltration ratio (front)	0.09	2.16	0.73	0.40	0.67	0.44–0.95
26	Myeloid inflt. ratio (front)	0.03	1.76	0.44	0.27	0.39	0.25–0.56
27	Deep IT lymphocyte fraction	0.00	0.96	0.39	0.24	0.35	0.19–0.56
28	Peritumoral immune richness	0.02	0.88	0.34	0.22	0.29	0.15–0.52
29	Immune desert fraction	0.00	0.41	0.03	0.06	0.01	0.00–0.03
30	IT myeloid–lymphoid tilt	0.00	1.11	0.08	0.16	0.02	0.01–0.08
31	Interface immune pressure	0.77	6.34	3.21	1.00	3.23	2.53–3.86
32	Invasion depth (p75)	–0.76	123.70	33.77	21.16	29.28	20.56–41.34
33	TC–Fib coupling (front)	2.79	4.81	3.56	0.36	3.53	3.31–3.76
34	TC–Ly NN distance (front)	1.96	5.71	3.95	0.56	3.96	3.65–4.26
35	Peritumoral Fib enrichment	0.38	1.28	0.72	0.14	0.71	0.63–0.79
36	Stromal inflammatory tilt	0.00	1.06	0.12	0.17	0.06	0.02–0.16
37	Fib–Ly proximity (stroma)	2.04	3.82	2.67	0.26	2.65	2.52–2.80
<i>(E) Spatial heterogeneity (log scale)</i>							
38	TC density heterogeneity	0.00	9.32	7.94	1.13	8.06	7.69–8.46
39	Ly density heterogeneity (IT)	0.00	9.45	4.63	2.77	5.37	4.44–6.34
40	Stromal cell. heterogeneity	6.46	9.01	7.68	0.45	7.66	7.38–7.97

Abbreviations: IT, intratumoral; S, stromal; T–S, tumor–stroma; Ly, lymphocyte; TC, tumor cell; Fib, fibroblast; NN, nearest-neighbor; Eos, eosinophil; Neu, neutrophil; CV, coefficient of variation.

Supplementary Table 11: Significant Spearman correlations per cancer type and molecular data type. Each cell shows the number of significant correlations (false discovery rate < 0.05 after Benjamini–Hochberg correction within predefined families) out of the total tested. Totals include all adjustment models. Significance rates vary with sample size: PANCAN ($n = 4,654$) and BRCA ($n = 953$) show the highest yield, while small cohorts (UCS, $n = 53$; CHOL, $n = 36$) have low power.

Cancer	n	Expression	CNV	Pathway	Immune	Total	%
ACC	52	370/ 10,640	0/ 10,640	139/ 4,000	62/ 480	571/ 25,760	2.2
BLCA	344	3,916/ 10,640	421/ 10,640	1,718/ 4,000	299/ 480	6,354/ 25,760	24.7
BRCA	953	6,547/ 10,906	2,967/ 10,906	2,735/ 4,100	346/ 492	12,595/ 26,404	47.7
CEC	259	1,052/ 5,320	1/ 5,320	444/ 2,000	83/ 240	1,580/ 12,880	12.3
CHOL	36	168/ 10,640	0/ 10,640	0/ 0	39/ 480	207/ 21,760	1.0
COAD	405	2,856/ 10,640	429/ 10,640	1,214/ 4,000	238/ 480	4,737/ 25,760	18.4
ESCA	141	890/ 10,374	0/ 10,374	254/ 3,900	92/ 468	1,236/ 25,116	4.9
HNSC	412	2,889/ 10,640	843/ 10,640	1,069/ 4,000	185/ 480	4,986/ 25,760	19.4
LIHC	328	3,543/ 10,640	217/ 10,640	2,080/ 4,000	317/ 480	6,157/ 25,760	23.9
LUAD	436	3,549/ 10,906	391/ 10,906	1,628/ 4,100	246/ 492	5,814/ 26,404	22.0
LUSC	319	1,948/ 10,640	125/ 10,640	930/ 4,000	178/ 480	3,181/ 25,760	12.3
MESO	71	616/ 10,640	0/ 10,640	312/ 4,000	102/ 480	1,030/ 25,760	4.0
OV	69	296/ 5,320	2/ 5,320	229/ 2,000	41/ 240	568/ 12,880	4.4
PAAD	129	187/ 10,640	3/ 10,640	116/ 4,000	33/ 470	339/ 25,750	1.3
PRAD	316	1,113/ 5,320	7/ 5,320	598/ 2,000	63/ 240	1,781/ 12,880	13.8
READ	138	778/ 10,906	111/ 10,906	282/ 4,100	99/ 492	1,270/ 26,404	4.8
STAD	353	3,159/ 10,906	545/ 10,906	1,381/ 4,100	208/ 492	5,293/ 26,398	20.1
THCA	452	5,501/ 10,640	669/ 10,640	2,274/ 4,000	348/ 480	8,792/ 25,760	34.1
THYM	116	1,638/ 5,320	58/ 5,320	720/ 2,000	81/ 200	2,497/ 12,840	19.4
UCEC	407	777/ 5,320	120/ 5,320	466/ 2,000	95/ 240	1,458/ 12,880	11.3
UCS	53	1/ 5,187	0/ 5,187	2/ 1,950	0/ 234	3/ 12,558	0.0
PANCAN	4,654	8,854/ 10,906	5,800/ 10,906	3,397/ 4,100	420/ 492	18,471/ 26,404	70.0
All	–	50,648/203,085	12,709/203,091	21,988/72,350	3,575/9,112	88,920/487,638	18.2

Supplementary Note 2: Cross-Endpoint Replication of Survival Associations

To assess the robustness of overall survival (OS) findings to endpoint definition, we evaluated replication across three secondary endpoints: disease-specific survival (DSS), progression-free survival (PFS), and disease-free survival (DFS). Starting from the 60 feature–cancer pairs that reached $FDR < 0.05$ for OS (unadjusted model), we asked how many also reached $FDR < 0.05$ for each secondary endpoint, with hazard ratio direction matching OS (Table 12).

Supplementary Table 12: Cross-endpoint replication of OS-significant survival associations. Replication requires the same HR direction and $FDR < 0.05$ for the secondary endpoint. DFS is excluded from per-pair counts because it was not available in the `get_endpoint_concordance` output for this analysis.

Endpoint	Available pairs	Replicated (<i>n</i>)	Replication rate
OS (reference)	60	60	100%
DSS	59	37	62.7%
PFS	60	32	53.3%
DSS & PFS	59	29	49.2% ^a

^a Fraction of pairs with both DSS and PFS available that replicated in both secondary endpoints simultaneously.

OS/DSS concordance is inflated by overlapping event definitions. Overall survival and disease-specific survival share a similar event definition (death from any cause vs. death attributable to cancer), differ mainly in the censoring of non-cancer deaths, and are computed from overlapping follow-up windows. Consequently, the 62.7% DSS replication rate overstates true biological cross-validation; the two endpoints are not independent. The 53.3% PFS replication rate provides a more conservative, clinically orthogonal measure of reproducibility, as PFS captures disease recurrence and progression rather than mortality.

Direction concordance without significance threshold. Among the 60 OS-significant pairs, all DSS-replicated and PFS-replicated associations agreed in HR direction with OS. When we relaxed the FDR threshold and examined direction alone (regardless of DSS or PFS significance), a larger fraction of associations pointed in the same direction across endpoints, consistent with genuine biological signal attenuated by reduced event counts in secondary endpoints. Attenuation is expected because DSS and PFS event counts are systematically lower than OS event counts in most TCGA cohorts (especially in cancer types with good long-term prognosis, such as BRCA and THCA), reducing statistical power below the FDR threshold even when the underlying effect persists.

Feature-level patterns. Associations with the strongest OS effect sizes showed the highest replication rates across all endpoints. For example, *intratumoral lymphocyte density* replicated for both DSS and PFS in BRCA, HNSC, and the pan-cancer analysis; *intratumoral apoptotic index* and *tumor pleomorphism index* replicated across all three endpoints in LIHC; and *mitotic index* replicated for both DSS and PFS in MESO. In contrast, associations with OS effect sizes near the FDR threshold ($HR \approx 0.80$ – 0.85) frequently failed to reach significance for PFS, consistent with power limitations rather than directional inconsistency.